Ku-Band Ultra-High Resolution Radar Tomography of an Alpine Snowpack

Ryan Natale Bartley

A thesis submitted to the faculty of
Brigham Young University
in partial fulfillment of the requirements for the degree of

Master of Science

David G. Long, Chair
Wood Chiang
Cameron Peterson

Department of Electrical Engineering

Brigham Young University

ABSTRACT

Ku-Band Ultra-High Resolution Radar Tomography of an Alpine Snowpack

Ryan Natale Bartley
Department of Electrical Engineering, BYU
Master of Science

A commercial-off-the-shelf Ku-band Frequency Modulated Continuous Wave (FMCW) synthetic aperture radar (SAR) system is coupled with a custom built two-dimensional scanning system. This system is installed in an alpine environment and pointed at a snow-unstable mountain slope for the duration of a Utah winter. The radar scanning system, designed to be capable of mapping a snowpack and its layers, is employed to create a series of three-dimensional images from a remote location. Individual images demonstrate the ability to directly detect snow layers, Furthermore, successive images are compared to track volume magnitude and phase values over the course of winter, including many snow deposition and melt events. The digital signal processing techniques used to create a high-resolution voxel (a three-dimensional pixel) map describing these snow layers is discussed. Results are discussed and further work is suggested for improving upon the results of this work.

ACKNOWLEDGMENTS

TABLE OF CONTENTS

LIST OF TABLES

LIST OF FIGURES

ix

CHAPTER 1.   INTRODUCTION

1.1   Purpose

Snow avalanches are among the most powerful forces on earth. The most devastating form of avalanches can exert forces over 10 tons per square meter and move at speeds greater than 100 m/sec [7]. If someone is in the avalanche's path, there is little time to escape and few structures capable of withstanding the oncoming force. According to the Colorado Avalanche Information Center's website, which tracks avalanche data for the entire United States, over the years 2007 to 2017, an average of 27 people per year were killed by the avalanche that overtook them [8]. Of the recorded avalanche events in history, there have been single events that have killed thousands of people [9]. It is unknown exactly how many lives could have been saved from better predicting avalanche events, but it is safe to say that better forecasting can save lives in the future.

Current forms of data gathering for avalanche forecasting are dangerous, labor-intensive, empirical and arguably antiquated. Forecasting involves a combination of weather watching, snow deposition measurements, infrared imaging and/or snow pit observation - the most reliable, and easily the most dangerous, being the latter of these methods. Even when this task is performed to the best available degree, snowpack density, water content and crystalline structure within a small area have large variations due to microclimates [4, 10–23]. As a result, comprehensive forecasting for a single area requires a prohibitive number of samples.

To reduce avalanche risk, authorities employ brute force solutions to create frequent, and therefore small, avalanches to mitigate risk. This involves triggering an avalanche through some form of explosion. For example, Utah Department of Transportation (UDOT) uses Gazex and Obell'X systems which rely on propane and hydrogen, respectively, to create explosions to trigger avalanches. Theses systems rely on a finite energy source and require helicopters to refill their tanks. The most common method, however, is the use of World War II era US Army surplus Howitzers which fire an explosive round capable of throwing shrapnel up to 1,000 meters from

the point of impact [24]. The danger associated with these systems was made clear in 2005 when a 105 mm Howitzer round overshot the intended slope and struck a home in a neighboring town. Luckily no one was injured, although a portion of a home was destroyed [25]. Because of the risk of current mitigation techniques, and due to the risk and ineffectiveness of current forecasting, a better method of forecasting is needed.

This thesis outlines the design and implementation of a high resolution Ku-band Linear Frequency Modulated Continuous Wave (LFMCW) radar system to aid in the forecasting of avalanches by collecting volumetric information on a selected snowpacks. By collecting data with a two-dimensional synthetic aperture, a three-dimensional image (tomographic image) of the snowpack is created. The Ku-band (15.5 GHz to 17 GHz) radar signal interacts with the snow from the snow-air boundary (top) to the snow-ground boundary (bottom), to provide information about crystalline structure within the snow volume. This expected interaction is discussed herein. Using the collected data, observations of snowpack conditions can be made to contribute to the forecasting of avalanches.

1.2 Contribution

This thesis contributes to the use of synthetic aperture radar for the intent of snowpack interrogation and, ultimately, avalanche forecasting. Radar systems have been employed extensively in the past for the purpose of assessing Snow Water Equivalence (SWE), dielectric constants, absolute depth and/or layer thickness. The intent of this work, however, is to evaluate volumetric properties of a snowpack using penetrating radar observed from a distance. While this purpose in and of itself is not novel, the techniques and tactics employed are.

This work is an extension to the novel work performed by Preston in 2010 [4], who created a primitive scanning device and successfully performed tomographic, or three dimensional, imaging using a C-band radar to assess volumetric scattering. On the suggestion of both [4] and [12], and because of Ku-band's ability to both penetrate snow and interact with smaller structures, a Ku-band system is used in this follow-on work. The intersection of the aforementioned reasons and the availability of a high-resolution Ku-band system was also a major driver in the radar selection.

We evaluate Preston's suggestions and respond to lessons learned. An entirely new scanner is designed and built which better handles environmental conditions. The scanning device has a

larger extent which enables larger radar apertures and, as a result, greater capability. Also possessing greater capability is the selected radar, an IMSAR NanoSAR B, which is capable of a range resolution of 10 cm. The finished system is then installed at a semi-permanent site, with shore power and Ethernet, which permitted collections over the duration of an entire winter.

1.3 Outline

The thesis is comprised of 5 chapters. The first chapter, of course, is the introduction. The following chapters are as follows:

- Chapter 2 reviews prior art and describes key differences between past experiments and the effort at hand. Lessons learned, resulting in design decision for a new system are noted. The backprojection algorithm is review and it's specific application to this effort is discussed.

- Chapter 3 reviews the scanning and radar system designs. Both radar and scanning system requirements are formulated and addressed. A design is developed, manufactured and tested.

- Chapter 4 outlines the data collection process and reviews the results. Imagery is formed at coarse and fine resolutions. Change detection images are formed as well. System strengths and shortcomings are presented.

- Chapter 5 concludes the thesis. Future improvements and future study suggestions are discussed.

CHAPTER 2.   BACKGROUND

The following section discusses the details of Linear Frequency Modulated Continuous Wave (LFMCW) radar and the backprojection image processing algorithm. Prior art on the topic of radar based snowpack imaging, tomographic radar and radar/snow interaction is presented.

2.1   Linear Frequency Modulated Continuous Wave Radar

The IMSAR NanoSAR B used for the project is an LFMCW Ku-band radar, which necessitates a discussion on the theory of such a system. This form of radar has been well understood for decades though, so only a light review is needed. Topics discussed include the radar range equation, time of flight, range resolution and azimuth resolution.

The most fundamental equation of radar is the Radar Range Equation (RRE). The NanoSAR B is a coherent radar, meaning that both amplitude and phase are recorded during collection, and then employed during processing. The Signal-to-Noise RRE for a coherent system using pulse compression and integrating across n_p pulses is

$$SNR_c = \frac{P_t G_t G_r \lambda^2 \sigma n_p}{(4\pi R)^3 R^4 k T_0 FBW} \tau_{swp} B \; , \tag{2.1}$$

where the terms are:

- P_t, Transmitted power (w)

- G_t, Transmit antenna gain (dB)

- G_r, Receive antenna gain (dB)

- λ, Carrier wavelength (m)

- σ, Target Radar Cross Section (RCS) (m^3)

- R, Standoff range to target (m)

- k, Boltzmann's constant (1.38064852 $10^{-}23$)

- T_0, Standard noise temperature (290 K)

- F, Noise figure of system (dB)

4

- *BW*, Receiver bandwidth (Hz)

- n_p, Number of pulses coherently integrated

- τ_{swp}, Transmit pulse length (s)

- *B*, Pulse modulation bandwidth (Hz).

For this effort, many of the terms above are fixed due to equipment constraints, such as antenna gain, pulse length, transmit power, and wavelength. However, some parameters have flexibility, such as transmit bandwidth and number of pulses. The RRE along with its parameters are addressed in the Radar Requirements Section.

The LFMCW system, like all other radars, depends on the most basic principle of Radio Detection and Ranging (RADAR), which is time of flight. By measuring the time, τ, it takes for a known signal to travel from the radar to a target and then back, the range, *R*, to the target can be derived, remembering that this time represents a two-way time:

$$R = \frac{c_0 \tau}{2} \, , \tag{2.2}$$

where c_0 is the speed of light in a vacuum. Here, c_0 is explicitly called out as being in a vacuum, as *c* varies with the medium which that light travels through, as is discussed later.

When compared to a traditional pulsed system, the LFMCW radar relies on a long pulse over which the transmitted signal is linearly ramped from one frequency, f_1, to another, f_2, over a given time, τ_{swp}, and centered around some center frequency, f_0. The total frequency swept is known as the bandwidth, *BW*, while the rate at which the full bandwidth is traversed is called the ramp rate, β. Fig 2.1 illustrates an LFMCW transmit and receive pulse frequency vs. time.

Once the pulse has been transmitted, reflected off a target and traveled for a total τ seconds, the energy is received as a time delayed copy of the transmit signal. This received copy is "de-chirped", meaning it is mixed with the transmit sweep, resulting in a sum and difference frequency. This signal is then low-pass filtered, preserving only the difference frequency, or intermediate frequency, f_{int}. With this information, τ can now be calculated using

$$\tau = \frac{f_{int}}{\beta} \, . \tag{2.3}$$
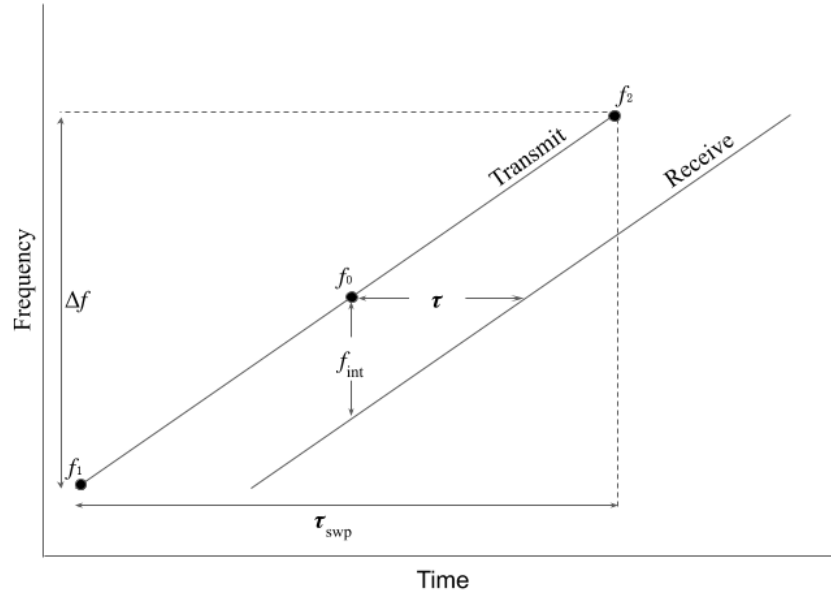
Figure 2.1: Example LFMCW radar timing. The frequency sweep from f_1 to f_2, centered at f_0 for a single sweep which lasts τ_{swp} seconds. The received signal from an ideal point scatter occurs τ seconds after transmission

Furthermore, by substituting Eqn. 2.3 into Eqn. 2.2, we now have a complete equation to find range to the target:

$$R = \frac{c_0 f_{int}}{2\beta} \, .$$

(2.4)

When rearranged, Eq. 2.4 provides the f_{int} frequency based on the range to target

$$f_{int} = \frac{2\beta R}{c_0} \, ,$$

(2.5)

which is useful in our discussion on resolution. It is important to note that the output of an ideal single, stationary target, is a sinusoidal tone.

Before moving on, one more radar system parameter must be discussed - the Pulse Repetition Frequency (PRF). The PRF of a system is the reciprocal of the Pulse Repetition Interval (PRI), or the time interval from the start of one pulse to the start of following pulse. For a simple LFMCW system, no more than one pulse is "in flight" at a time. If this principle is violated the resulting

data contains range ambiguities that degrade the signal utility. This means that when imaging at great distances the PRF must be lower than when imaging at close distance.

Furthermore, when performing SAR imaging from a moving platform, a pulse must be emitted once every $l/2$ (which is the length of the antenna in the azimuth direction) to satisfy the Spatial Nyquist Sampling requirement. So the faster the antenna moves, the higher the PRF must be. [4] The PRF for this experiment is not a concern due to the relatively short ranges and slow movement of the radar.

2.1.1 Resolution

Resolution is a fundamental characteristic of a radar system. It describes the minimum distance at which two identical objects need to be separated to be distinguishable. The Rayleigh Resolution Criterion (RRC) objectively defines resolution as the distance from the peak of the first object to the first null of the second object. To derive the range resolution of an LFMCW system, we first must imagine two tones received using Eq. 2.5, which is visualized in the right of Fig. 2.2. Now referencing the left of Fig. 2.2 we see that the spacing from peak-to-null of a *sinc* is $1/T$, where T is the observation period of the *rect* in the Time Domain. This information, coupled with Eq. 2.5, allows us to set up the inequality which represents the Rayleigh Criterion

$$\frac{1}{T} = \frac{2\beta R}{c_0} \quad , \quad BW = T\beta \ .$$

(2.6)

When solving for R, we must recognize that this is the minimum range at which two points are distinguishable, which equates to the range resolution

$$\delta_{rng} = \frac{c_0}{2BW} \ .$$

(2.7)

While LFMCW radar inherently provides high range resolution, it must be coupled with processing techniques to provide high resolution in orthogonal directions, such as azimuth and elevation. Because the NanoSAR B is coherent, and because we precisely know the location of the moving antenna for each pulse, we can create a synthetic aperture. The advantage of a Synthetic Aperture Radar (SAR) system is that it can provide a finer azimuth resolution than a real-aperture
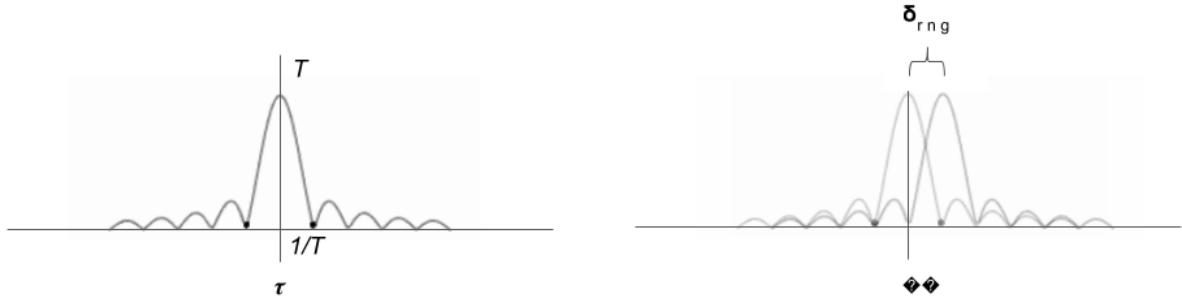
Figure 2.2: Transformation of a *rect* in Frequency Domain is a *sinc* with peak-to-null width of $1/T$ (*left*). Illustration of Rayleigh Resolution Criterion (*right*)

system. For SAR, azimuth resolution is also independent of range, given that the system can provide full support and has sufficient power. A target achieves full support when it is viewed across an integration angle, θ_{int}, equal to the size of the azimuth beamwidth. In other words, the target is sampled for the length of an entire synthetic aperture, D_{SAR}, as can be seen in Fig. 2.3. When a full synthetic aperture is formed, the effective minimum (finest) azimuth resolution is

$$\delta_{az} = \frac{l}{2} \, , \tag{2.8}$$

where l is the length of the real aperture in the azimuth direction. When only a partial aperture is formed, the more general form of azimuth resolution must be applied [4, 26],

$$\delta_{az} = \frac{\lambda R}{2D_{SAR}} \, , \tag{2.9}$$

where λ is the wavelength at the center frequency. While a partial aperture still provides a finer resolution than a real-aperture system, the resolution is no longer independent of range, and thus
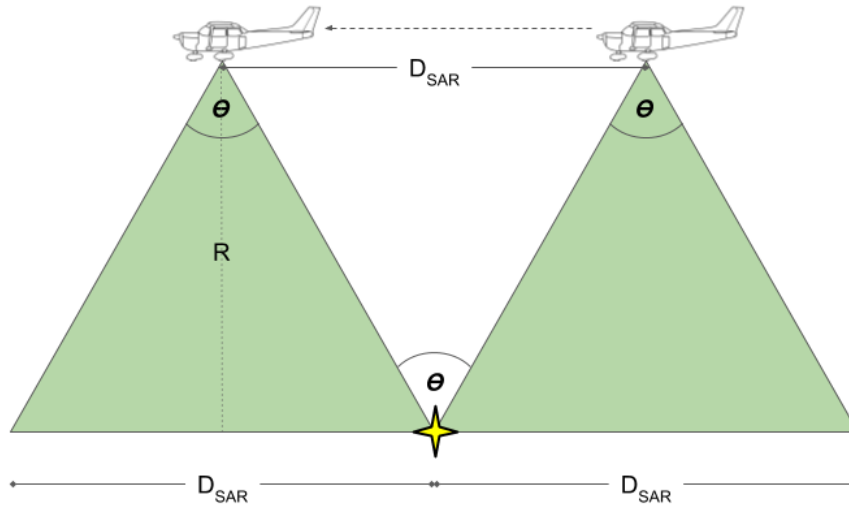
Figure 2.3: Transiting a full aperture, D_{SAR}, results in the target being viewed across the full beamwidth , θ, and provides the maximum azimuth resolution

coarsens with increased standoff range, R. Reducing the synthetic aperture length, D_{SAR}, has a similar effect to increasing the range.

The concept of creating a large synthetic aperture, and thus a narrow synthetic beam, in the azimuth direction results in a fine azimuth resolution. This idea can easily be extrapolated to the elevation direction. By creating a synthetic aperture in the elevation direction, while doing the same in the azimuth direction, a narrow pencil beam is realized. These apertures are created by "dragging" the antenna in their respective directions as shown in Fig. 2.4. The same requirements and equations (Eqn. 2.8 & Eqn. 2.9) discussed for azimuth resolution also apply to the elevation dimension. Using fine range resolution, as a result of large transmit bandwidths, and fine azimuth and elevation resolutions, as a result of large synthetic apertures, results in a fine resolution voxel (a voxel being the three-dimensional analog of a pixel) which, in turn, makes possible high resolution three-dimensional imaging. This resolution is obtained by combining pulses taken from different locations within the aperture and then applying signal processing techniques such as the backprojection algorithm.
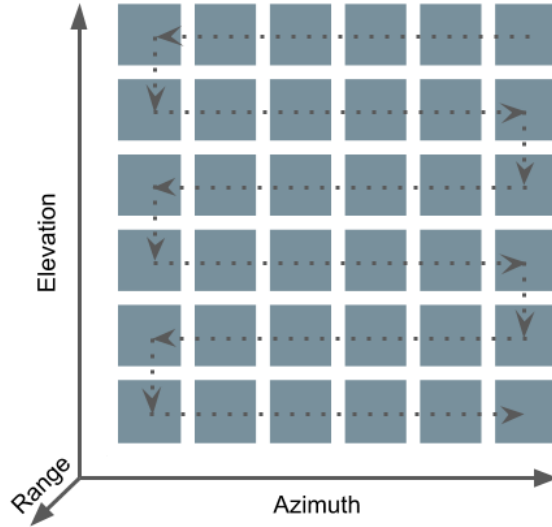
Figure 2.4: Diagram of a two dimensional synthetic aperture scan. A synthetic pencil beam is created by dragging the radar in space along the azimuth and elevation directions. Range resolution is a function of bandwidth as discussed in the text.

2.2 Backprojection Algorithm

The Backprojection Algorithm (BPA) is a simple yet powerful time-domain processing algorithm. The BPA requires no assumptions about geometry or imaging mode and, as such, can be applied to nearly any imaging situation. It compensates well for non-ideal radar motion, and when antenna and target locations are known exactly, it is the ideal image formation algorithm. Conversely, the BPA is computationally intensive and imprecise knowledge of the target and antenna location introduces image artifacts [27, 28].

In order to create an image using the BPA, a summation must be performed across each pulse (n) and each voxel location (x_0, y_0, z_0) within the synthetic aperture. The output of a single iteration of the BPA, A, is the magnitude and phase of the reflected energy from the specified voxel for a single pulse, and is calculated using

$$A(x_0, y_0, z_0) = P(d[n]) \exp\left\{ j4\pi \frac{d[n]}{\lambda} \right\}, \tag{2.10}$$

10

where x_0, y_0, and z_0 are Cartesian Coordinates whose origin is arbitrary, but constant. The function $P()$, which resides within Eqn. 2.10, retrieves the magnitude and phase from the range compressed pulse at a specified standoff range

$$d[n] = \sqrt{(x-x_0)^2 + (y-y_0)^2 + (z-z_0)^2},$$ (2.11)

which requires precise knowledge of the antenna phase center (x, y, z) and the pixel location (x_0, y_0, z_0) for the nth pulse.

Precise knowledge of $x, y,$ and z can be provided through many means (as evident in later chapters), but the most common is a GPS and Inertial Measurement Unit (IMU) combination. How the voxel location is decided upon varies depending on the imaging mode. For two dimensions, looking at Eq. 2.11, (x_0, y_0) are selected based on antenna pointing, while z_0 can be assumed using a flat earth approach or, when available, a Digital Elevation Map (DEM) of the area of interest. For three dimensions, the values of z_0 are no longer a single plane, but are now multiple planes. Instead of assuming a single plane along the ground is being imaged, the tomographic image is created using mutliple planes, creating a volume above and/or below the ground.

When considering Eq. 2.10 for a three dimension image, it can easily be seen how computationally intensive backprojection image formation truly is. Assuming the image is a cube, as in Fig. 2.5, the voxel element count can easily be in the thousands. For example, a radar capable of a 1 meter cubic resolution, imaging a volume 10 meters per side requires 1,000 voxels. Each voxel requires completion of the BPA values for each pulse. A data collection using a radar with a PRF of 1 KHz, such as the NanoSAR B, and lasting an hour has roughly 3,600,000 pulses. In total, completion of a 10 x 10 x 10 tomographic image requires 3,600,000,000 iterations. Each iteration requires a square root and matched filter which are both considered computational inefficient operations.

Due to the advancements in processing power, such as Graphics Processing Units (GPU), computational limitations are no longer a major limiting factor. As a result, the BPA has become more common in image formation. Location accuracy is still a concern, however, as measurements are still not, and most likely will never be, perfect. There are several methods for removing the effects of these inaccuracies, such as auto-focus, although these are outside the scope of this ef-

5 cubes per side | 125 total cubes   10 cubes per side | 1000 total cubes
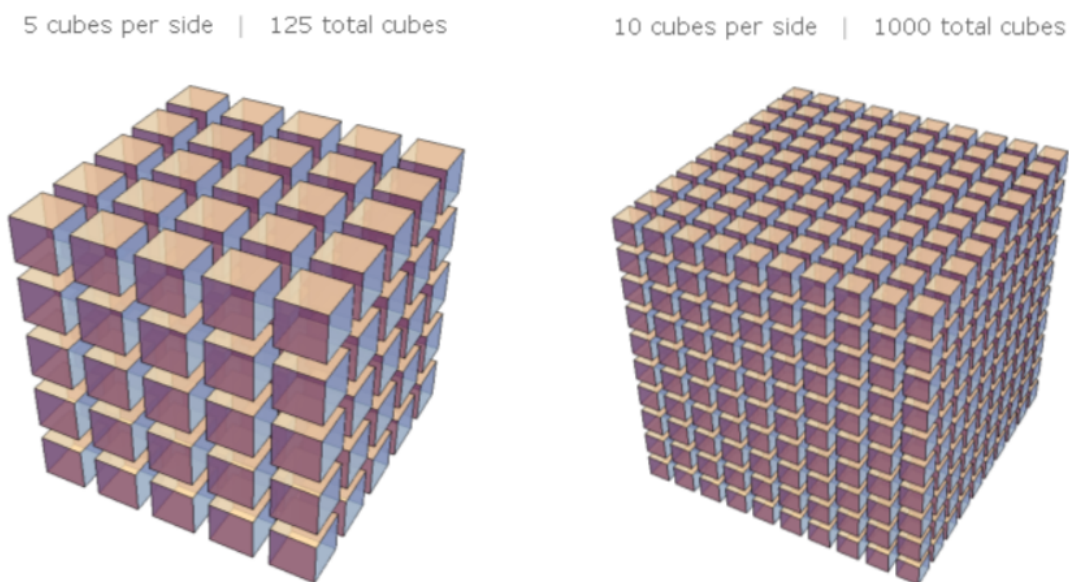
Figure 2.5: Visualization of voxel image cube and demonstration of complexity for three-dimensional image formation. Image cube on left has 5 voxels per side, while image on the right has 10 voxels per side.

fort. For a more detailed examination of errors, their effects and how to overcome them look to Duersch's work in [27].

2.3 Prior Art

Snowpack observation has only been a relatively recent application for radar. Before the 20th century, only a limited number of observational studies had been performed. During this time period, the most significant development was the connection of snow layering, or stratigraphy, and resultant avalanche behavior. It was not until the mid-20th century that a significant amount of resources were dedicated towards snow observation. And it was not until 1979 when radar was first used to observe a snowpack [13].

Since 1979, a multitude of studies have been performed that used some form of radar to observe one or more aspects of a snowpack [3, 4, 10, 12, 14, 15, 17, 18, 20–22, 29–37]. Radar has become a common measurement tool due to the non-destructive nature of interrogation and its ability to observe several characteristics of a snowpack, such as stratigraphy, density, snow water

equivalent (SWE), reflectivity, permittivity (ε_0) and crystalline structure. Also, due to the nature of the transmitted electromagnetic waves, it is capable of penetrating to great depths. Finally, radar can cover large areas and more easily reach remote locations depending on deployment method.

Flexibility in adjusting parameters is desirable aspect of radar. Depending on what the experiment aims to observe, the facilitator can adjust frequency, bandwidth, polarization, antenna orientation and/or geometry. Adjusting one or more of these parameters can dramatically change the outcome of the collection and enable extraction of various geophysical parameters of interest.

The primary consideration when using radar is the transmitted frequency. The two main effects of frequency are penetration depth and particle interaction. Unfortunately these two properties are diametrically opposed: a lower frequency penetrates to greater depths but primarily interacts with larger particles, while a higher frequency interacts with small particles but can lack penetration depth. This is an unfortunate paradigm because it is desirable to penetrate a snowpack as deep as possible while observing the crystalline structure of the snowpack, which is on the order of centimeters or less. As a result there is a large breadth of frequencies used in radar snowpack studies. Several studies have used P (~200 MHz), L (~1 GHz) and S (~2 GHz) band systems to maximize observable depths [10, 14, 16–18, 21–23, 32, 34, 35, 37–39]. In attempts to find a middle ground of penetration vs particle interaction intermediate bands have been used, such as C (~5 GHz), X (~10 GHz) and Ku (~18 GHz) [3, 4, 11, 15, 16, 18, 20, 29–31, 33, 36, 40]. A few studies, in search of ultra-fine resolution, have implemented millimeter wave frequencies such as Ka-band (~35 GHz) [20, 30]. Limited research at higher frequencies is most likely due to the limited penetration and dearth of available technology.

For each of the LFMCW systems [3, 4, 12, 14, 15, 17, 18, 20, 21, 29–37] maximizing bandwidth was important in order to reduce resolution, which meant higher fidelity measurements. Resolutions varied from a fine as 1.4 cm [18] to as coarse as 3 m [37], although this number naturally trends to finer resolution over the course of the 30+ years of academic research that this effort references. Very few system have used fully polarimetric radar systems [10, 35, 37, 39]. Those that did, noted substantial differences between single-pol and cross-pol products but none identified the significance, although there was speculation. For the most common geometry, a polarimetric system does not make much difference, as the radar was situated directly on, and normal to, the snowpack [3, 10, 12, 17, 20–22, 29, 31, 32, 34, 35]. Even fewer systems were airborne [14, 18, 29, 35, 37],

13

which aside from the obvious benefits of reaching remote locations and covering large areas, is difficult due to the added uncertainty in positional accuracy. And, like the system designed and implemented herein, a handful of systems were ground-stationary, looking at the snowpack from a distance [4, 30, 33, 36].

Another driving factor in parameter selection is the location of the data collect. Generally speaking, locations can be split in to two main categories: Arctic/Antarctic regions and Alpine regions. Arctic and Antarctic regions present a simpler scenario, in that they generally remain cold year round and there is very little foliage, resulting in simple, homogeneous snowpack [3, 17, 18, 21, 22, 32, 39]. Conversely, alpine climates have temperatures which fluctuate dramatically, daily and seasonally, and foliage is typically abundant leading to extremely variable and complex snowpacks [4, 10–16, 18–21, 23]. Because of the relative simplicity of the Arctic and Antarctic regions, assumptions can be made in an to attempt to bound the problem. For example, Kanagaratnam, et al. [32] were able to justify the assumption of a constant density and ε_0 (with an associated uncertainty) in Northern Greenland because of a-priori knowledge on the homogeneity of the icesheet. With this assumption, they were able to estimate icesheet layering and overall thickness to within 5%, at depths exceeding 200 m, where previous measurements were four times more uncertain. Where a snowpack was more variable, higher-order assumption were necessary, such as with Ellerbruch et al. [29] who used a multiple-order ε_0 curve in order to measure SWE. However, this study required an independent measurement of total snow height to create a determined solution. Unfortunately, to create a system with an exact solution one or more of the variable which we seek to estimate must be measured, making remote observation a difficult task.

Much of the prior art available performed two dimensional imaging of the snowpack. While two dimensional imaging provides a profile view of the snow stratigraphy, three dimensional imaging, known as tomography, provides additional information about a snowpack's volume. Additionally, tomography covers substantially more area and allows transects of the volume along arbitrary planes. Examples of both forms of imagery can be seen in Fig. 2.6. Of the tomographic studies cited herein, a very limited number have attempted to interpret volumetric signatures, as opposed to layer boundaries, [4, 20, 32, 35, 37], and when narrowing the criterion to alpine environments the number of studies reduces to even less [4, 35].
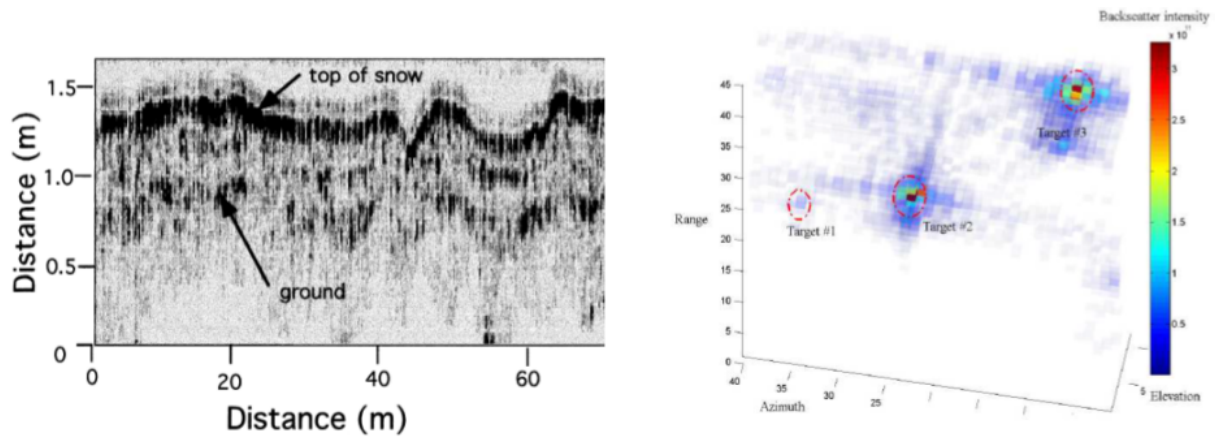
Figure 2.6: Two dimension profile of snowpack provided by [3] (*left*). Three dimensional radar image, known as tomography, provided by [4] (*right*).

2.3.1 Snow Structure and Radar Relationship

In order to tie measured radar backscatter to avalanche forecasting, it is important to understand how a snowpack's physical properties affect Electromagnetic (EM) propagation and backscatter. The most impactful properties of snowpack are liquid water content, ice crystal content and structure, air content and density. Various permutations of these properties can cause a vast shift in the resultant properties, which are dielectric constant (ε'), dielectric loss (ε'') and reflectivity.

According to Heilig et al. [10] there are four basic categories that a snowpack may fit in to with respect to water content. These are moist, wet, very wet, and slush with $< 3\%$, 3 - 8%, 8 - 15%, and $> 15\%$ liquid water content, respectively. Dry snow, which is a subset of moist, is considered to have less than 1% liquid water content.
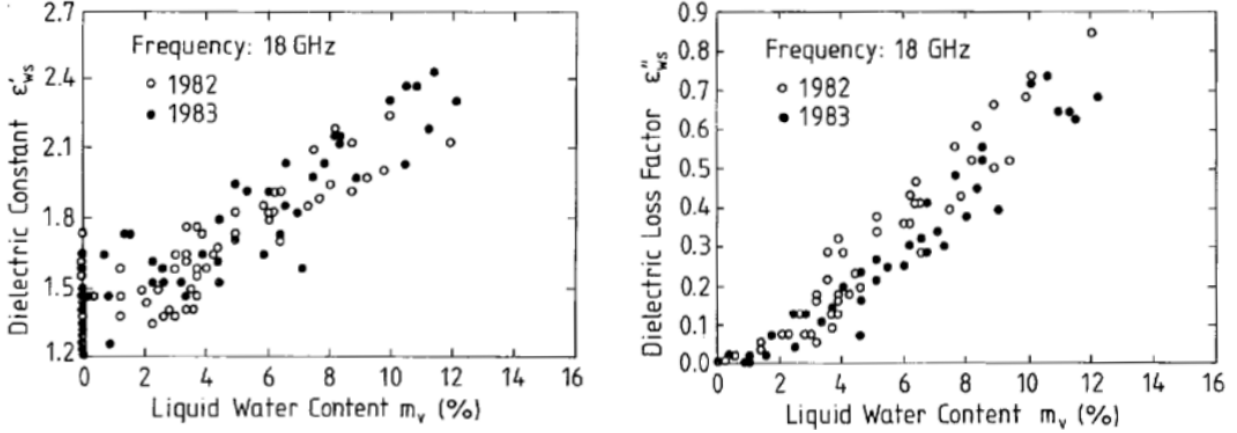
Figure 2.7: Dielectric constant and dielectric loss factor of snow measured at 18 GHz by [5] at varying liquid water contents.

Dry snow can be simply modeled as a mixture of air and ice. As a result, dry snow has a dielectric constant, ε', that can be modeled by

$$\varepsilon' = (1+0.845\rho)^2, \tag{2.12}$$

where ρ is the density of the dry snow in g/cm^3 [17]. Because dry snow has little to no water content it has a dielectric loss, ε'', that is effectively zero. This fact holds true for frequencies under 18 GHz [5]. Dry snow can have a density range of less than 0.1 g/cm^3 to 0.5 g/cm^3, resulting in a electric permittivity range of 1 to 2.02 [14, 17, 21, 31, 35]. As water content starts to exceed 1% the spectral behavior starts to become dominated by the dispersional behavior of water, removing the simplifying assumptions.

The remaining snow categories, e.g., moist ($>1\%$), wet, very wet and slush, are much more complicated mediums. This is because they have both an ε' and ε'' which contribute significantly to their electromagnetic response. Furthering complexity is the shape of the water inclusion (Pendular vs Funicular Regimes), which plays a role in the lossiness, or lack thereof, of wet snow and varies considerably with water content. Unlike dry snow, wet snow does not have a single, commonly accepted model for estimating the ε' and ε''.

Hallikainen et al. discuss six different wet snow models in [5]. These models are the 1) Two-phase Polder-Van Santen Model, 2) Three-phase Polder-Van Santen Model, 3) Confocal

16

Ellipsoidal Model 4) Refractive Model, 5) Empirical Model based on Linlor's Formulation and 6) Debye-like Semi-Empirical Model. Each model requires some level of empirical measurements to tune fitting constants. Example empirical data is displayed for 18 GHz in Fig. 2.7. Furthermore, each model comes with associated benefits and draw-backs, such as limited applicable frequency ranges or greater root mean squared errors. Hallikainen concludes that the closest fit is a modified Debye model which was shown to be applicable from 6 GHz to 37 GHz.

This discussion would be incomplete without discussing the effects of a snowpack's crystalline structure on slope stability and radar backscatter. The remainder of this subsection presents a brief introduction on these topics - for a much more detailed and thorough discussion look to Preston in [4]. A slope's stability can be reduced to the interaction of individual layers with neighboring layers, so understanding particle cohesion is important. While radar backscatter is dependent on dielectric properties (discussed above) and individual and collective Radar Cross Section (RCS) and incidence angle. These properties can be better understood by taking a closer look at common snow grain shapes and sizes.

The crystalline structure of a snow grain can be described as faceted or round, each with several sub-categories. Faceted snow grains are angular structures. The most common, and most dangerous, form of faceted snow is hoar snow, with surface hoar and depth hoar being the most common forms. These layers are created by large temperature gradients which form at the ground-to-snow or snow-to-air interface. These are among the most dangerous formations because they have weak cohesion among other grains, and as such, are typically referred to as "sugar snow". A depth hoar that has formed unseen, or a surface hoar the gets buried by snowfall or wind events, creates a weak layer that can be easily overburdened by layers overhead. The overburdening and eventual shearing of these layers is what causes large avalanches. Round snow grains are a much more stable structure because they have more surface area for a given size, allowing for more and stronger bonds, and because they can be tightly packed together. [4]

A collection of mostly homogeneous snow grains constitutes a layer. This can be composed of surface hoar, depth hoar or round particles as discussed above. Other common layers are snow crusts and wind deposits. Snow crusts are hard, dense layers that are typically created by a melt/freeze cycle or rain event. Due to their insulative nature and their tendency to capture moisture, crusts aid in the creation of hoars. Relatively speaking, crusts are a smooth layer which

presents a weak point within the snowpack due to low cohesion with neighboring layers. This smooth layer also acts as a specular plane and tends to create large amounts of forward scatter. Wind depositions are created by settled blowing snow. These layers are notorious for forming quickly, on the order of minutes, and being extremely dense. Snow depositions create uneven and heavy layers that can easily cause overburdening of lower layers and are, thus, considered extremely dangerous. [4]

2.3.2 Volume Scattering

As stated previously, many radar snow studies have endeavored to study boundary information, while few studies have attempted to extract information about the snow volumes. Experiments intending to study boundaries naturally collected normal to the boundary layers, which creates strong specular backscatter off of the the layers while drowning out the faint reflections of the volumes between layers. In order to reduce the received signal from the layer boundaries, the snowpack must be view at an angle off of normal. This concept is critical when penetrating a snowpack because ground returns can often dominate all other returns. Marshall et al. suggest in [12, 15] that incidence angles less than 30° are required to avoid intense ground reflections. This phenomenon is illustrated in Fig. 2.8 and is the result of Snell's Law.

Snell's Law of Reflection states that the angle of reflection is the same as the angle of incidence. These two angles are θ_1 and θ_1' in Fig. 2.9. Snell's Law of Refraction provides a relationship between incidence (θ_1) and refraction (θ_2) angles in terms of a ratio of phase velocities, which is:

$$\frac{sin(\theta_2)}{sin(\theta_1)} = \frac{n_1}{n_2},$$
(2.13)

where n is the refractive index and is defined as the ratio of the phase velocity in free space to the phase velocity in the medium, which reduces to

$$n = \sqrt{\varepsilon_r} \quad , \quad \varepsilon_r = \varepsilon' + j\varepsilon''.$$
(2.14)

For dry snow the refractive index is a real value, while for wet snow it is complex. When the refractive index of the incident medium is less than that of the entered medium, i.e., $n_1 < n_2$, then
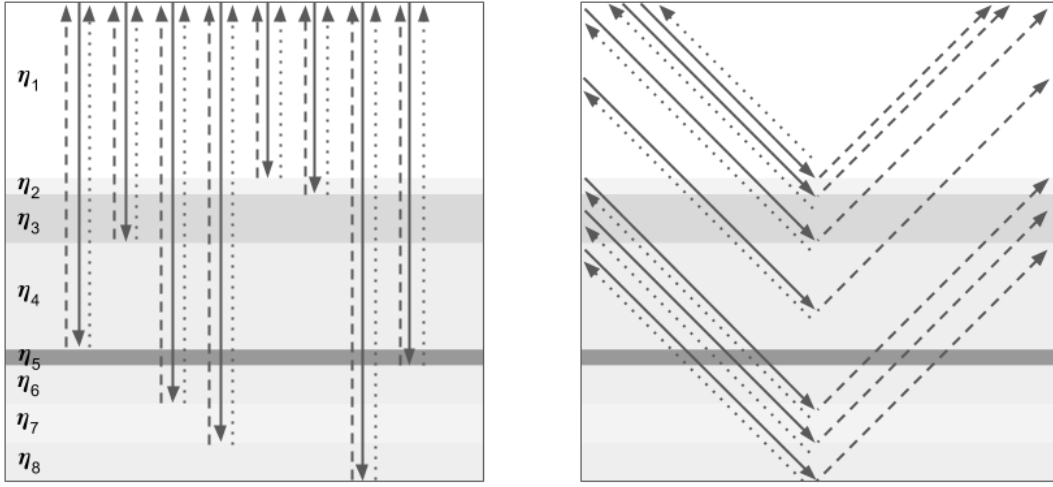
Figure 2.8: Simplification of snow stratigraphy represented by various thicknesses and refractive indexes, *n*. Incident waves (solid lines) enter normal to snowpack, where faint returns (dotted lines) are mixed in with strong returns (dashed lines) (*left*). Incident waves enter from left at approx 45°, faint returns return back to the radar, while strong returns forward scatter (*right*).

$\theta_2 < \theta_1$. Conversely, when $n_2 < n_1$ then $\theta_1 < \theta_2$ [6]. Marshall et al. in [11] found that when the snow layer depth was on the order of a wavelength or less, the layer depth had substantial influence on the reflected and refracted waves. In addition the layer thickness, the relative roughness, again when compared to the transmitted wavelength, of the surface must be considered.

When an incident wave intersects with a more complicated surface, such as that in the right side of Fig. 2.9, the response is also more complicated. Because the mediums boundary is rough, there are many surfaces, each with a different angle, with which the incident wave interacts. Snell's Law still applies here, effectively once for each surface, which for all intents and purposes can be considered countably infinite.

All of the reflected and refracted energy must obey the Law of Conservation. Thus, the refracted and reflected wave for each incident wave carries with it some coefficient, such that

$$\tau = 1 + \rho, \tag{2.15}$$
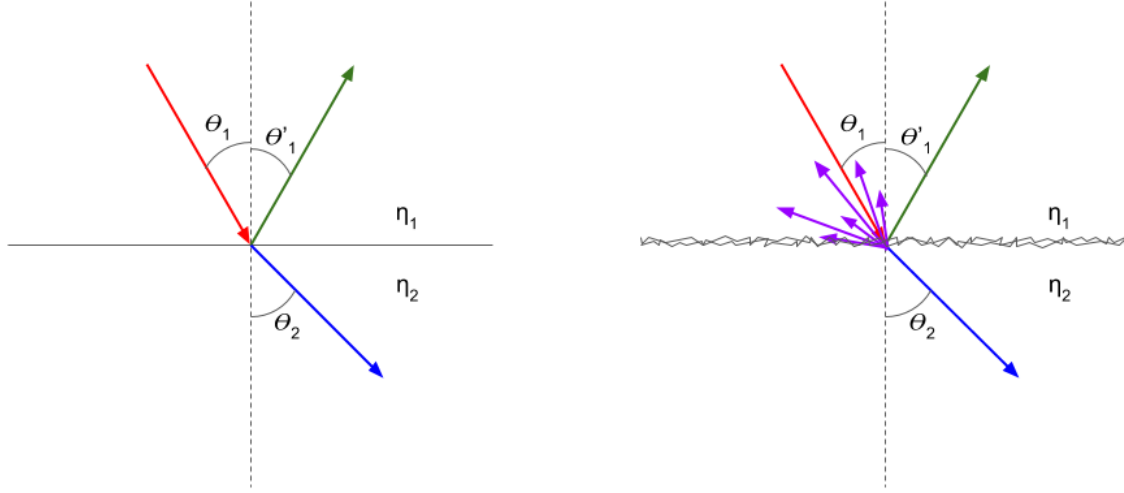
Figure 2.9: Snell's Laws for a specular surface. Incident wave travels through the first medium with refractive index, n_1, at θ_1 and enters the second medium with refractive index n_2 at a new angle of θ_2 (*left*). Snell's Laws for a rough surface such as snow. In addition to reflection and refraction, backscatter is created, shown in purple, due to rough surface (*right*).

where τ is the transmission coefficient and ρ is the Fresnel coefficient. The Fresnel coefficient is represented in terms of the wave impedance's, η, of the two mediums ($[n_1, \varepsilon_1]$ and $[n_2, \varepsilon_2]$)

$$\rho = \frac{\eta_2 - \eta_1}{\eta_2 + \eta_1} , \tag{2.16}$$

where η_i can be a real or complex number (depending on water content, as discussed above), and is calculated using

$$\eta_i = \sqrt{\frac{1}{\varepsilon_i' \varepsilon_0}} (1 - j\frac{\varepsilon_i''}{\varepsilon_i'})^{-1/2}, \tag{2.17}$$

for the ith layer in question [6].

The power with which the incident signal is reflected is a function of the volume backscattering coefficient, σ_v. The value of σ_v is the accumulation of scattered energy from individual contributors, which for simplification is modeled as spheres, within the volume. This value can be

estimated using

$$\sigma_v = \sum_{i=1}^{N_v} \pi r^2 \xi_b \ , \tag{2.18}$$

where N_v is the number of particles in the volume, r is the average radius of the particles and ξ_b is the backscattering efficiency. For the sake of simplicity, scattering is assumed to operate in the Rayleigh Regime (as opposed to the Mie Regime). This means that particle sizes are assumed to be 2.0 mm or less, which is a reasonable assumption for snow flake size [4], for an incident wave centered around 16.25 GHz. As a result, The backscattering efficiency can be reduced to being a function of the normalized circumference, χ, and the index of refection, n,

$$\xi_b = 4\chi^4|K|^2 \ , \quad K = \frac{n^2-1}{n^2+2} \ , \tag{2.19}$$

where K can be a complex value [6]. This equation will be necessary to complete the radar range equation, which will be calculated for this system later.

2.4 Conclusion

The LFMCW radar system is a well understood radar system, with a well defined set of basis equations. These equations will be put to use in the following chapters to substantiate the design of an LFMCW radar system for snow avalanche study. Upon collection of radar data, the backprojection algorithm will be used to create a three dimensional image comprised of hundreds to thousands of voxels.

The backprojection algorithm is also a well understood concept. The BPA has had limited use due its computationally expensive nature. However, due to advancements in processing this is no longer a limitation.

Neither the LFMCW radar nor the BPA are novel in and of themselves, but have not previously been combined in this manner. As explained above, radar is the ideal method for studying snow stratigraphy. However, most studies have focused on boundary discovery, layer thicknesses and total snowpack depth. Few studies have looked to study the volumes in between boundaries. Only one study, which happens to be the basis for this thesis, has attempted to link volume mea-

surements to avalanche behavior. Thus there is a need to further our understanding of volumetric radar signatures, their properties, and how it is related to avalanche behavior.

CHAPTER 3.   SYSTEM DESIGN

3.1   Motivation

This chapter describes the design of a two-dimension scanning Synthetic Aperture Radar (SAR) system which aids in the remote sensing of snowpacks and their layers. By remotely interrogating a snowpack and identifying unstable and dangerous layers, avalanche experts are able to more safely and more accurately forecast avalanches. In order to be effective, the radar must be able to sufficiently penetrate the snowpack and form high resolution, three-dimensional imagery, which avalanche experts can then analyze.

In order to realize this outcome, the radar system must be capable of forming a synthetic aperture in both azimuth and elevation to satisfy the requirement of creating a three-dimensional, or tomographic, image of the snowpack. To do so, a two-dimension mechanical scanning device is created to form these apertures, such that the resolution is made finer in post-processing. Furthermore, the radar must have a large transmit bandwidth to satisfy the need for fine range resolution. The result are high-resolution voxels, as discussed in Chapter 2 above, at and below the surface of the snow to create, in effect, tomographic images of the snow pack.

In order to increase our chances of success and optimize the utility of data collected for this experiment, an appropriate site must be selected. Located in an alpine environment, the scanner is weatherized so it can operate throughout the entirety of a winter, collecting data often.

With the collected data, the time-domain backprojection algorithm (BPA) is used to transform raw data into high resolution tomographic images of the snowpack. Because data is collected often, the progression of snow deposition, settling and/or melting can be tracked and identified in the tomographic images. By observing this progression, differences in the various layers of the snowpack are revealed. This information is related to slope snow stability and aids in avalanches forecasting.

Parameter	Value
Waveform	LFMCW
Center Frequency	16.25 GHz
Bandwidth	500 MHz and 1500 MHz
PRF	1 kHz
Duty Cycle	83%
Transmit Power	1 Watt
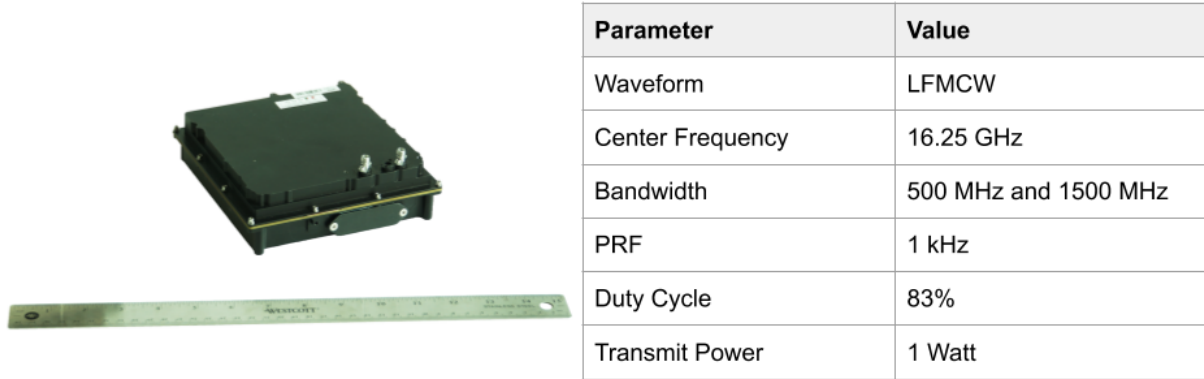
Figure 3.1: IMSAR's NanoSAR B displayed next to a ruler for scale (*left*). Summary of NanoSAR B operational parameters used in this study (*right*).

3.2 Radar Requirements

The radar system design starts with a review and assessment of the terms of the RRE presented in Eq. 2.1. While the scanner design is influenced by the past work reviewed in Chapter 2, it draws heavily on the work performed by Preston in [4]. Furthermore, it is important to note that while there is flexibility in design parameters, there are several constraints due to the availability and expense of high quality imaging radars.

One such constraint is on the frequency band selection. For this project IMSAR LLC generously one of their radar units. This radar, known as a NanoSAR, operates at Ku-band with a wavelength of approximately 1.8 cm. Per the discussion in Chapter 2, Ku-band provides a suitable middle-ground of penetration and particle interaction and, as a result, is the desired band for this effort. The Ku-band NanoSAR is capable of transmitting between 15.2 GHz and 17.2 GHz (wavelength of 1.97 cm to 1.74 cm). An image of the NanoSAR B and a summary of the specifications selected for this effort are provided in Fig. 3.1.

The NanoSAR Ku-band radar has several adjustable parameters and several that are immutable. The immutable parameters are inconsequential to this effort due to radar system being stationary, but are necessary to compute our expected SNR and consequently are discussed briefly. These parameters are the PRF, which is fixed at 1 KHz, and τ_{swp}, which is fixed at 830 microseconds. The noise figure is approximately 2.7 dB. The adjustable parameters are transmit bandwidth and transmit power.

In order to collect the highest resolution data possible the transmit bandwidth must be maximized. The NanoSAR B is capable of achieving 1500 MHz of transmit bandwidth. Using Eqn. 2.7 this equates to a 0.1 meter slant range resolution. The bandwidth can be reduced to 500 MHz, or 0.3 m slant range resolution, to increase SNR and coverage area. Although the center frequency is software configurable, it is programmed to 16.25 GHz for the entirety of this study.

Two transmit power levels are readily available. Fortunately, both are calculated to provide more than enough power as seen below. The available Power Amplifiers (PA) provide 15 dBm and 30 dBm, or 32 milliwatts and 1 Watt respectively. To evaluate the required transmit power, the substantial loss incurred by penetrating wet snow should be considered. For Ku-band this value can range from near zero for snow with no moisture to hundreds of decibels per meter for wet snow. Figure 3.2 represents the calculated absorption coefficient using the Debye-like model [6].

Standard gain horn antennas are used for both transmit and receive due to their availability and relatively low cost. The selected horns are Narda Ku-band (12.4 GHz to 18.0 GHz) antennas with WR-62 waveguides. At the average center frequency for this study, 16.25 GHz, the gain of the antennas is approximately 17 dBi. The 3 dB antenna beamwidth is 26° for both azimuth and elevation. The antennas are mounted such that orientation can be easily adjusted to allow for collection at various polarizations. According to [41], vertical polarization does not present statistically different backscatter properties than horizontal polarization, while the cross-pol products (HV-pol) present a much lower backscatter coefficient, σ. Consequently, for this collection, the transmit and receive are oriented for horizontal polarization.

Although Ulaby's σ_0 measurements provides insight into the reflectivity of the surface of the snow, the volume backscatter, σ_v, must be considered when the volume of snow is of interest [41]. Referring to Eq. 2.18, the volume backscatter coefficient, σ_v, is estimated for a voxel using the anticipated dimensions of 0.1 m x 0.1 m x 0.1 m. Using the density of snow provided earlier
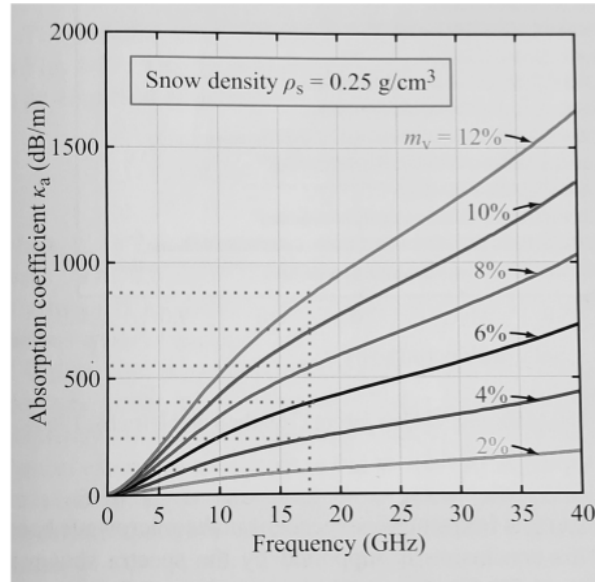
Figure 3.2: Absorption coefficient by frequency and snow water content using Debye-like model. Assumed snow density of 0.25 g/cm^3. Chart courtesy of Ulaby and Long [6].

(0.1 g/cm^3 to 0.5 g/cm^3), the number of particles, N_v, within the volume are estimated. The complex index of refraction, n, is then approximated from the graph in Fig. 2.7. The resulting output for σ_v is displayed in Fig. 3.3.

To complete the RRE several other values are needed. The one-way slant range, R, is constrained to be no greater than 2,000 meters. This is a conservative estimate as range variation significantly impacts the SNR due to a $\frac{1}{R^4}$ factor. The final term is the number of pulses, n_p, that are coherently integrated. This number is addressed further in Section 3.3 below, but an appropriate assumption for now is 60,000 (equivalent to 60 seconds worth of data). With values for all terms addressed, the output of the RRE, Eqn. 2.1, is displayed in Fig. 3.4.

Still referencing Fig. 3.4, the NanoSAR radar coupled with a 1 Watt power amplifier provides ample SNR for SAR imaging across a wide range of particle sizes when using the commonly accepted value of 15 dB for SAR imaging. When considering snow loss, this is not always the case. With snow loss factors exceeding 500 dB per meter at Ku-band with 12% snow water content, this system - or any reasonable system - is insufficient for penetrating wet snow. Therefore, the effort
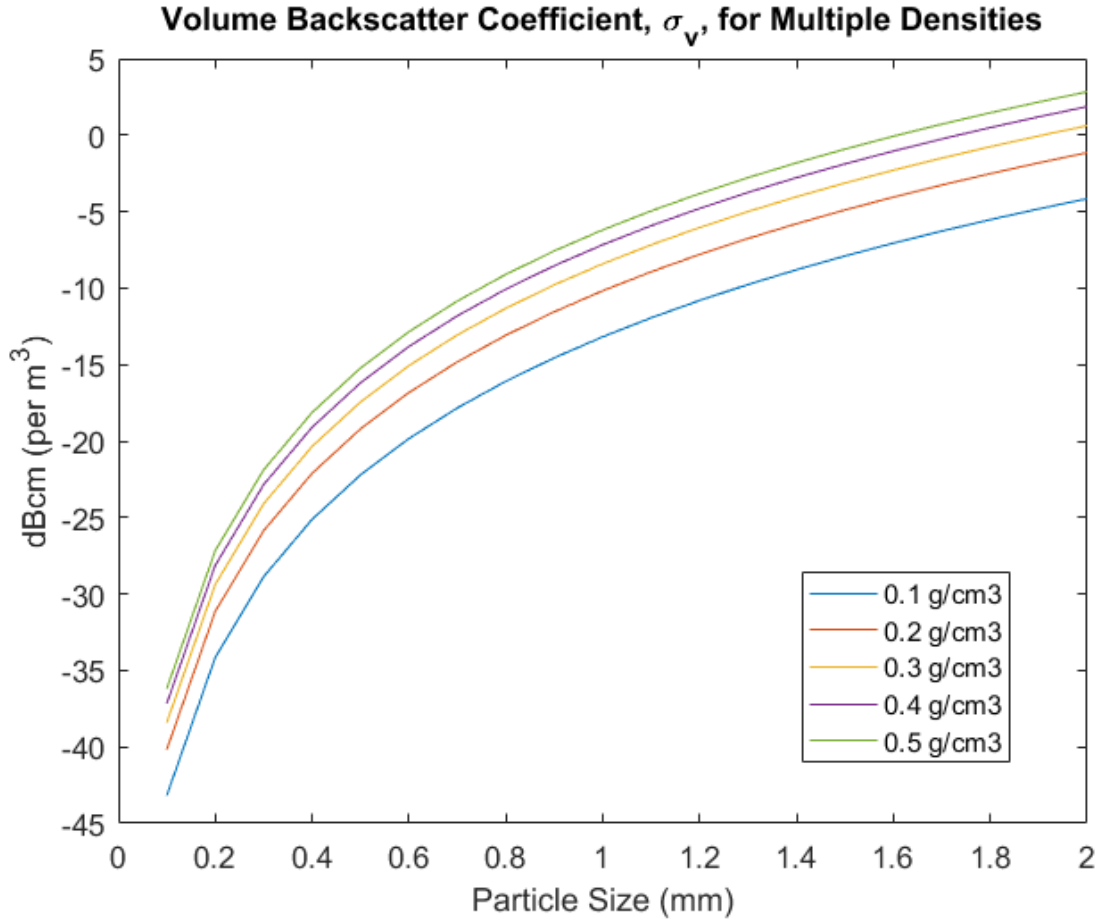
Figure 3.3: Volume backscattering coefficient, σ_v, for a range of particles sizes and multiple discrete densities.

herein is constrained to imaging mostly dry snowpacks. This is not an unreasonable expectation for a high alpine Utah snowpack.

3.3   Scanner Requirements and Design

Image quality is not only a function of radar parameters but is also a function of how the radar is employed. The radar parameters which enable high quality imagery were discussed in Chapter 2. In this section we discuss how these principles are applied through design parameter considerations for the scanning mechanism, referred to as the "scanner" herein. These considerations enable high quality remote three dimensional imaging.
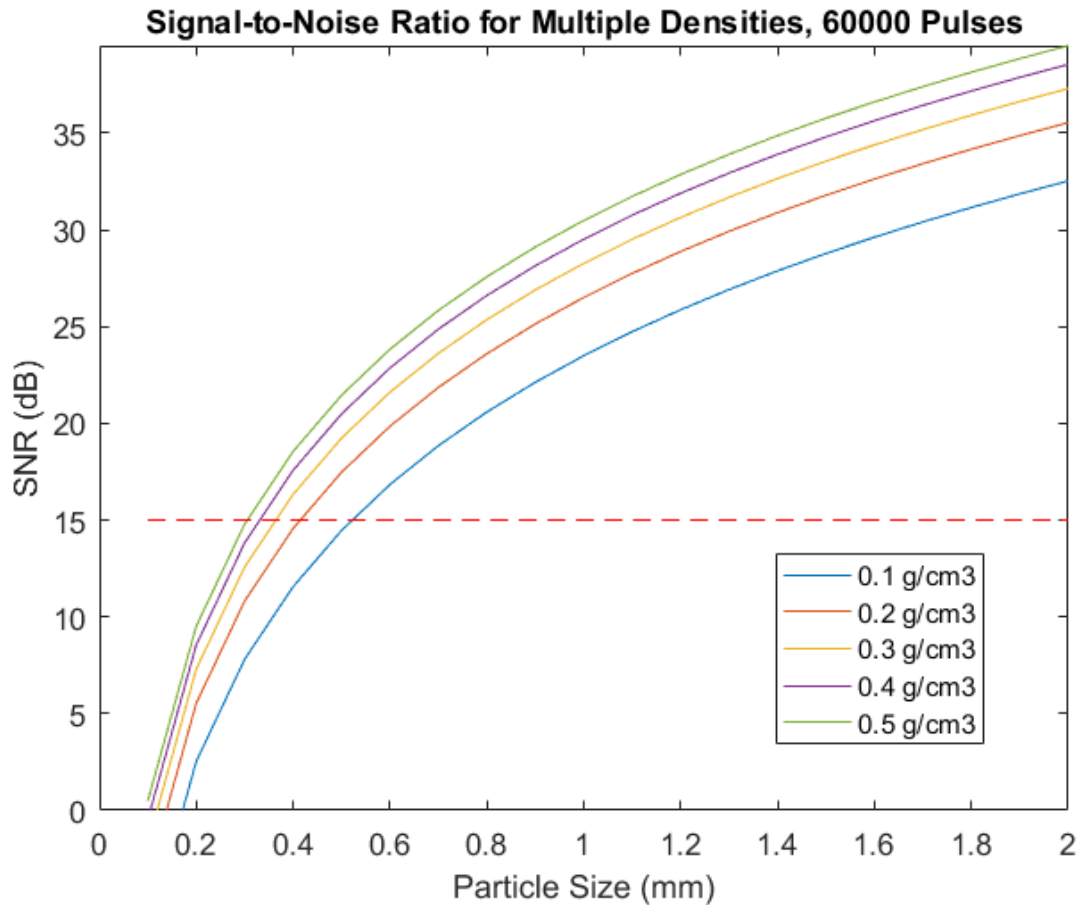
Figure 3.4: Output of the RRE, Eq. 2.1, using the terms discussed in Section 3.2. Values used assume that snow water equivalent is $< 1\%$, minimizing the loss factor. Assuming a minimum of 15 dB SNR for high quality imaging, the system provides enough transmit power for most particle sizes as indicated by the dashed line.

The primary purpose of the scanner is to move the radar antennas in two dimensions to create a two dimensional synthetic aperture. The length of each synthetic aperture dimension, how quickly it traverses the length, and how accurately its position can be measured are primary considerations. Secondary considerations include weather resistance, ease of installation, ease of operation, and cost effectiveness.

Ideally, the scanner is capable of creating a complete, or fully supported, aperture that matches the azimuth and elevation resolution to the range resolution at 0.1 m. Using Eq. 2.9 and solving for D_{SAR}, or the synthetic aperture length, achieving a resolution of 0.1 m at a slant range of 1,000 meters requires a synthetic aperture that is 92 m wide. This is not feasible from both a

logistical and utility standpoint. Due to height and width restrictions at the anticipated scanner location the scanner is restricted to 2 m high by 3 m wide, which results in scanning extents that are 182 cm high and 283 cm wide. The resulting resolutions at a range of 1,000 meters, the expected range at the selected site, are 5.07 meters in elevation and 3.26 meters in azimuth. These resolutions are admittedly less than ideal, but must suffice.

To prevent aliasing in the horizontal directions the scanner must move slowly enough such that a radar pulse is transmitted and received at least every half antenna width (4.4 cm). For the Narda antennas, this equates to roughly 22 m/s, which is far beyond the abilities of the scanner and, thus, is not a concern. To perform an entire rectangular scan, the scanner performs row scans and then steps up/down in the vertical direction; this is repeated until the entire rectangular area is traversed. The sample distance in the vertical direction must be less than half the antenna height which is roughly 2.8 cm. Both of these criterion are software configurable and are set well within these bounds such that the scene is substantially oversampled. The scene is intentionally oversampled to increase image SNR. A complete scan takes, on average, 60 minutes to complete which equates to 3,600,000 pulses. Due to the large beamwidth and relatively long slant range, this means that each pulse is illuminating every voxel within the imaging volume.

In order to move the radar within the scanner, displayed in Fig. 3.5, a horizontal gantry, imaged in Fig. 3.6, is placed on precision-milled rails providing movement in the z (vertical) direction. Motion in the x (horizontal) directions is facilitated through a rail-mounted sled within the gantry. A Global Position System (GPS) was considered for tracking location; however, as civilian GPS is only able to provide accuracies on the order of several meters only GPS timing is used, while position is provided using other means.

To provide radar position, each axis is outfitted with an US Digital optical absolute encoder. Encoders with 4,000 cycles per revolution are used to provide accurate reporting of the gantry and sled, which are driven by heavy-duty stepper motors capable of micro-stepping at 2,000 steps per revolution. Each full revolution of the stepper motor creates approximately 3 cm and 4 cm of movement in the z and x direction, respectively. A single step is approximately 7.5 μm in the z direction and 10 μm in the x direction. Precise measurement is paramount when performing SAR imaging as errors on the order of $\frac{\lambda}{2}$ or greater have a defocusing effect. The smallest wavelength
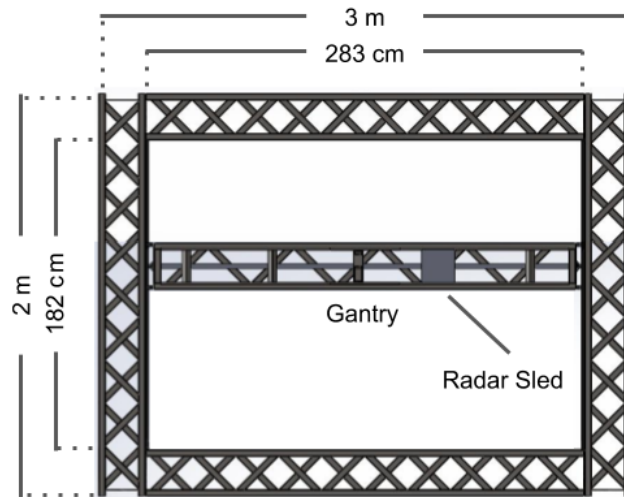
Figure 3.5: Diagram of the two-dimension mechanical system. The scanners external dimensions are 2 meters wide by 3 meters high. The radar scans within the structure and is restricted to 182 cm high by 283 cm wide. A radar sled resides on the gantry allowing for freedom in two dimensions.

Figure 3.6: Image of antennas and radar on the gantry mounted sled, all residing on the scanner gantry. Assorted RF, Ethernet, and power cables also shown.
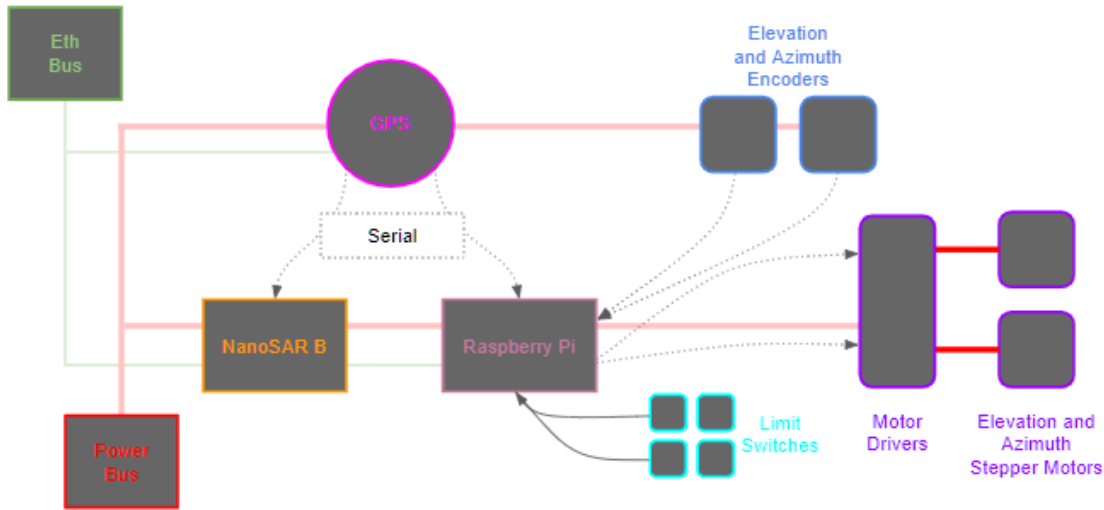
Figure 3.7: The Raspberry Pi SBC acts as the central nervous system for the scanner. It controls the radar, encoders, GPS and stepper motors. The Rapsberry Pi also accepts inputs from the GPS and encoders and fuses that information with the raw radar data which it transfers from the radar.

used during collection is 1.76 cm, which requires errors of less than 8.8 mm. The optical encoder error is substantially less than this.

These electrical subsystems (i.e., encoders, motors, gps, etc) are interconnected through various means. Referring to Fig. 3.7, the entire system is controlled by a Raspberry Pi Single Board Computer (SBC), outlined in light pink. When the system is powered on, the SBC configures the GPS module (maroon), encoders (blue) and stepper motors drivers (purple), all through RS 232 Serial connections. Upon initiation of a scan, the SBC first commands the the motors to home - this is done by moving to the x and z axes to their minimum and maximum extents, which is limited by two sets of switches (cyan). Once homing is complete, the scan commences, following the pattern in Fig 2.4. After the radar data is collected (approximately 500 Gb per scan), it is transferred from the radar to a mass storage device for post-processing.

As previously mentioned, the encoders (outline in blue in Fig 3.7) relay accurate location information to the Raspberry Pi which is then timestamped using the incoming GPS feed. Simultaneously, the radar is using the same GPS feed to timestamp individual radar pulses. Both the GPS module and encoder modules provide an update rate of 10 Hz, which then requires interpolation up to 1,000 Hz to match the PRF of the radar. With the location updates now matching the PRF, each pulse now has an accurate location.

31

Radar antenna position is further addressed by mechanical means. The scanner is rigidly designed, resulting in negligible deflection along all axes. This is made possible by using of heavy-duty steel trusses. This also addresses issues related to expansion and contraction caused by weather extremes, such as binding, but results in an extremely heavy structure (roughly one ton). This is a design issue that must be addressed in future systems as the installation required several people and a crane.

Recognizing that a major contributor to positional errors in a geared system is gear lash, careful design is implemented to reduce error to less than 1 cm. The scanner uses close-tolerance gears and high quality bearings, e.g., ABEC quality 5 bearings. Additionally, oversized axles and a rigid structure reduce slack in the system. While 1 cm exceeds the requirement by 13% it is near enough that image degradation should go unnoticed.

In addition to steel trusses and quality materials, further precautions are taken to withstand Utah winter weather. The radar sled and gantry are completely enclosed in a plastic housing with a hinged front. During each collection, the door is opened to limit excess feed-through which tends to be problematic in an enclosed LFMCW systems. Heaters are fixed to both ends of the gantry to heat internal items and the vertical rails, which have a tendency to accumulate ice that impedes vertical movement. Finally, multiple tool balancers are added to the gantry to accommodate the extra weight of accumulated snow and ice. The final configuration is illustrated in Figs. 3.8 and 3.9.

3.4 Site Selection

Site selection requires consideration of the scanner location and the observation location. The scanner location needs to be easily accessible (such that a crane can place the scanner), have access to power and Ethernet, and have a clear view of the observations site. For testing, the observation location should have plentiful snow and be void of foliage, the latter of which creates a simpler snowpack environment (as discussed in Section 2.3). Furthermore, the observation location should be less than 2,000 m (threshold), 1,000 m (objective), from the scanner location to ensure there is sufficient SNR. Ideally, the observation location is accessible by foot to allow for the gathering of truth data, though this was not the case for this study.
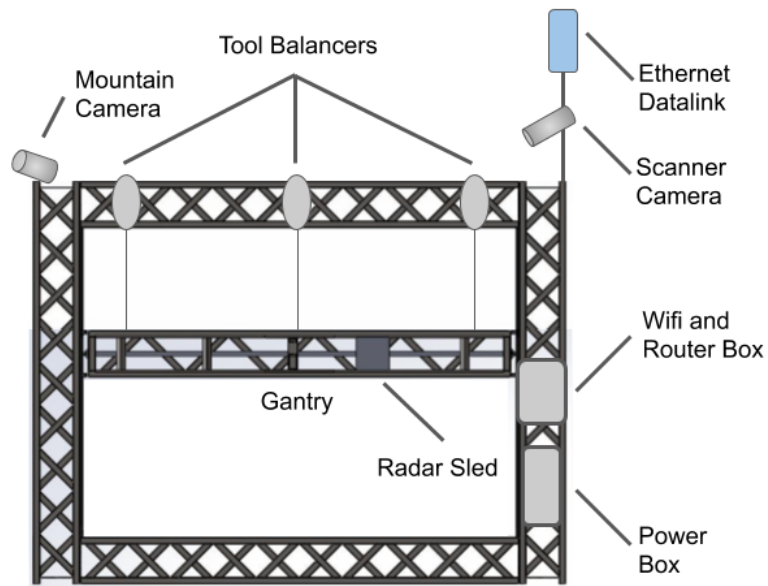
Figure 3.8: Front-view illustration of the scanner with auxiliary items such as full motion video cameras (to observe scanning and the mountainside remotely), tool balances, WiFi and Ethernet back-haul datalink.

Figure 3.9: Profile view of scanner at Aspen Grove, Utah (*left*). Rear view of scanner with observation site in the background (*right*).

Figure 3.10: The scanner and observation locations. The radars viewshed is highlighted in bright green wile the white trapezoid highlights the coverage area within the beamwidth. The intersection of these two areas represents the observable area.

Ultimately Aspen Grove, UT is selected as it meets most of the requirements and, most importantly, is available for our use thanks to Brigham Young University Facilities Management. The scanner site is easily accessible and provides shore power and Ethernet. The scanner is placed on a solid wood frame and pointed semi-permanently at the observation site, as seen in Fig. 3.9. A satellite view with the radar location, observation location, and radars viewshed is shown in Fig 3.10. The location is free of obstructions as can be seen in the profile view illustrated in Fig 3.11. The Aspen Grove site setup has a slant range of 650 m. This improves the resolution in azimuth and elevation to 2.12 m and 3.29 m, respectively. Furthermore, the shorter range also results in an increased SNR. The scanner orientation are illustrated in Fig. 3.12.

The observation site meets all but one of the discussed requirements. A preliminary assessment based on satellite imagery deemed the site suitable for this study, however, upon inspection in the Spring (post-collection) it was found to be covered in dense shrubbery that was roughly 0.5 m to 1 m in height. This has a significant negative impact on image quality, which is discussed in
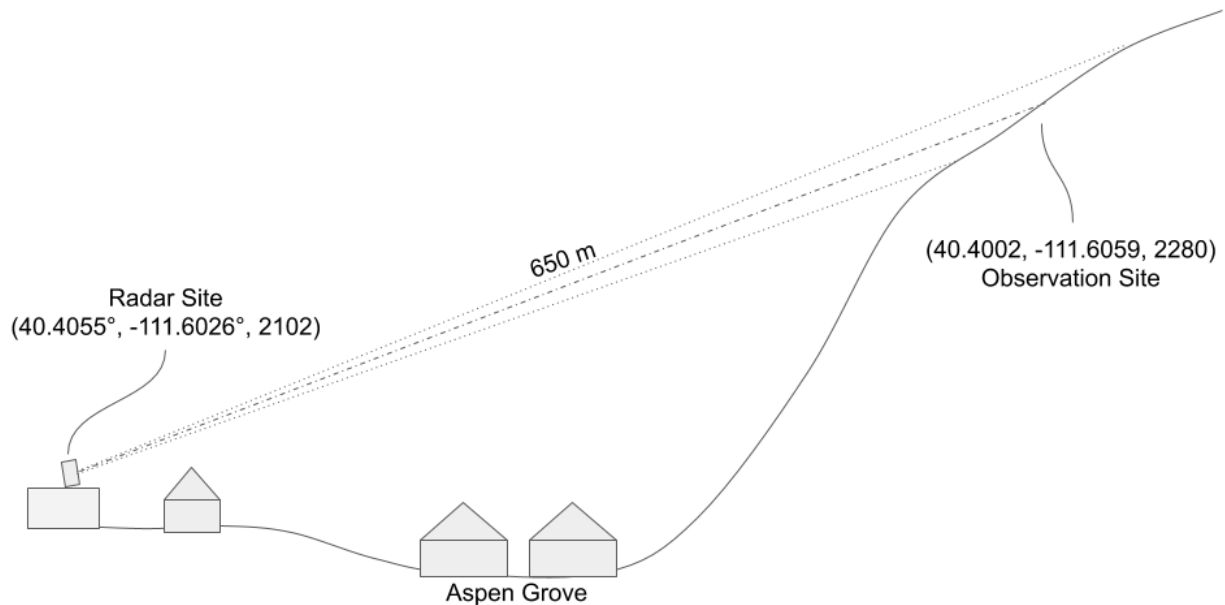
Figure 3.11: A profile view of the Aspen Grove site. The latitude, longitude and altitude of the scanner and observation center are provided on the left and right of the image. The approximate range between the two points is 650 meters.

Chapter 4. As Aspen Grove is located near Sundance Ski Resort, snow totals are available for the study period.

From 2010 to 2016, or five years prior to this study, Sundance had an average snowfall in excess of 3.65 m with an average base of 97 cm. This is sufficient for our collection purposes. However, as Aspen Grove is roughly 300 m higher in elevation than Sundance Ski Resort, a more substantial snowpack is expected. The 2016/2017 snowfall totals were reported at 6.75 m of total snowfall and an average snowpack of 1.8 m. There were a reported 26 significant snowfall events for the 2016/2017 winter - overall an excellent year for this data collection [1].

3.5 Conclusion

In order to create a high resolution tomographic images of an alpine snowpack, a complete scanning radar system is designed and built. The major considerations are the radar, scanning mechanism and site selection. Requirements for each of these components are discussed and adequately addressed in the final system.
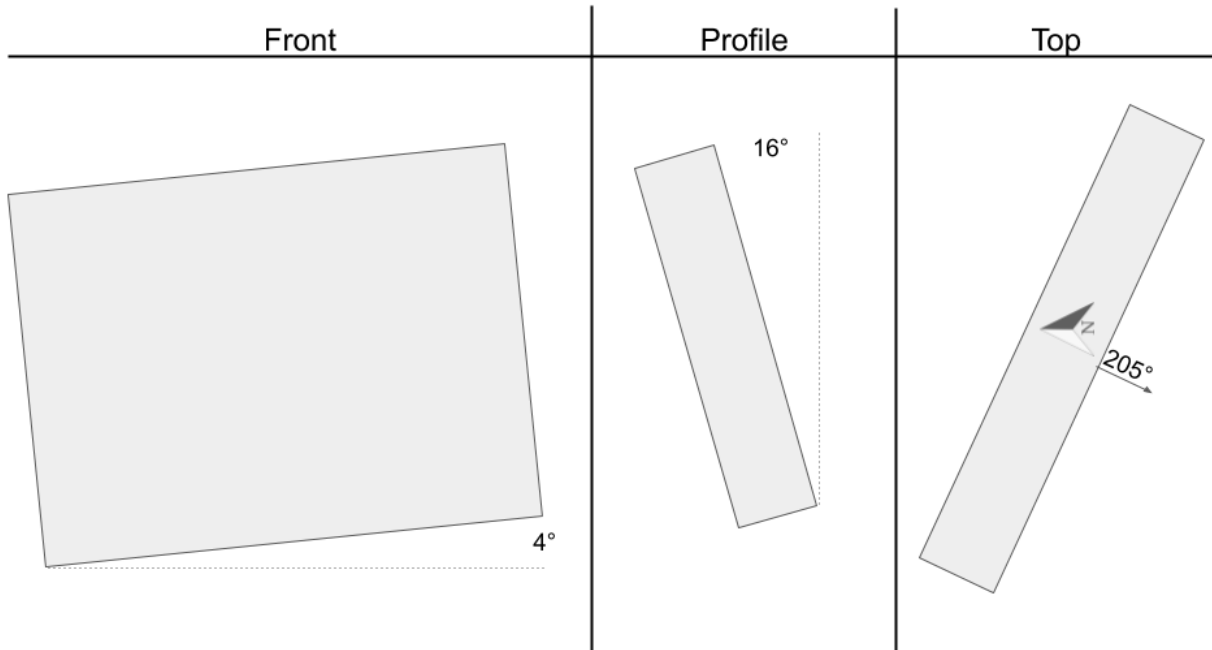
Figure 3.12: Scanner orientation at Aspen Grove.

The Ku-band NanoSAR B radar system is kindly provided by IMSAR LLC. The NanoSAR B meets requirements for range resolution and is at a desirable band. The radar is capable of high range resolution and when coupled to a 1 Watt power amplifier provides an acceptable amount of snow penetration and SNR.

The scanning mechanism meets most of the requirements to create high resolution three dimensional imaging. To create azimuth and elevation resolutions to match the high range resolution of the radar, the scanner would have to be unreasonably large. At 2 m tall by 3 m wide, the scanner allows moderate azimuth and elevation resolution. As is, the scanner is too large and too heavy for commercial purposes. The scanner is designed with heavy-duty materials to ensure it is rigid and, as a result, provides a precise location for each pulse transmitted.

The Aspen Grove radar site is easily accessible while the observation site is difficult to access in the summer and nearly impossible to access in the winter. The slant range is long enough to qualify for "remote sensing" and removes the scanner from any danger posed by an avalanche. The shorter slant ranges also allows for a higher SNR and finer elevation and azimuth resolution. Unfortunately, an error in setting the radar parameters caused the observation site to be less than

optimally place. The actual observation site is covered in dense foliage, roughly 0.5 to 1 m in height, which has a negative effect on data fidelity.

CHAPTER 4.   RESULTS

4.1   Data Overview

Radar data is collected over the course of the 2016-2017 Winter. Most of the collections are taken at the finest range resolution possible, of 0.1 m; however, several collects are performed at 0.3 m to increase coverage area and SNR. Of the 12 collections, the entire extents of the scanning mechanism are used in 10 of the collections which provides the finest azimuth and elevation resolutions possible of 2.12 m and 3.29 m, respectively.

Environmental conditions in between each collection and at the time of the collection are important to understand. The number of snow events and their magnitude ideally correlate to the stratigraphy present in the backprojected imagery. Snowfall information, in conjunction with temperature data, provide a better understanding of possible settling, melting, icing or crystal formation that may have taken place. Furthermore, the temperature on the day of the collect provides insight on current snow conditions.

A table of collection dates, parameters and environmental conditions are outlined in Table 4.1. The snowfall data, provided by onthesnow.com [1], is taken at Sundance Ski Resort which is roughly 300 m lower in altitude than the collection site and, as a result, will have different values than is present in the data. The temperature data, provided by NOAA [2], is taken at Alta Ski Resort which is similar in altitude, latitude and environment, e.g., an alpine canyon, to the Aspen Grove location.

The data collection location is approximately 650 m away from the radar location, shown in the right of Fig. 4.1, and is roughly 250 m higher in elevation. The imaging plane is complex due to a large amount of terrain relief. For example, when imaging within a 200 m cube, the terrain varies by as much as 100 m, as can be seen in the elevation map in the middle image of Fig. 4.1. To eliminate unnecessary calculations, voxels outside of plus-or-minus 20 m of the elevation map are omitted. Images at the finest resolution are only 20 m per side so all voxels are used. A large

Table 4.1: Overview of collections taken during the Winter of 2016-2017. In total 12 different collections were made, although only a select few are analyzed (green rows). The number of snow events and the depths of each event between each collection are provided by [1]. The temperatures between each collection are provided by [2].

#	Collection Date, 2017	Range Resolution	Snowfall Events**	Total Snowfall**	Avg. Snowfall**	Avg. Low Temp(℃)**	Avg. High Temp (℃)**	High Temp Day of Collect (℃)
1	Jan 28*	0.3 m	29	454.7 cm	15.7 cm	-10.2	-2.0	-2.2
2	Feb 5*	0.3 m	3	22.9 cm	7.6 cm	4.9	2.5	2.8
3	Feb 26, Collect 1	0.1 m	10	119.4 cm	11.9 cm	-6.3	1.9	-8.9
4	Feb 26, Collect 2	0.3 m	0	0 cm	0 cm	-6.3	1.9	-8.9
5	Mar 11	0.3 m	6	48.3 cm	8.0 cm	-7.7	0.7	6.7
6	Mar 19	0.1 m	0	0 cm	0 cm	0.8	11.0	12.2
7	Mar 24	0.1 m	1	7.6 cm	7.6 cm	-1.1	8.4	7.8
8	Mar 26	0.1 m	1	2.5 cm	2.5 cm	-6.1	3.6	2.8
9	April 4	0.1 m	2	20.3 cm	10.2 cm	-5.0	3.4	-1.1
10	April 9	0.1 m	0	0 cm	0 cm	-5.2	7.3	0.6
11	April 23	0.1 m	0	0 cm	0 cm	-3.1	7.5	10
12	April 30	0.1 m	0	0 cm	0 cm	-6.1	0.2	4.4

*Incomplete datasets
**Values since previous collection, first value represents values since first recorded snowfall (12/9/2016)

swath in elevation is necessary to account for inaccuracies in the Digital Elevation Model (DEM). A site profile is illustrated in the left of Fig. 4.1 to show the terrain relief.

Unfortunately, the data collects do not all have the same minimum slant range (corresponding to near swath) and so do not cover the same area. This complicates, and in some cases makes impossible, comparing successive images to identify changes. Luckily, several of the collections have at least some portion of their image swath overlapping. Furthermore, there was no snowfall beyond collection 9. As such the Results Section focuses on collections 4 through 9. The selected collections present a wide range of conditions, from no snow events to heavy snow events and from cold weather to warm weather.

In order to interpret the images displayed in the following sections, it is necessary to understand the image orientation. The x axis aligns with the east/west directions, the y axis aligns with the north/south directions and z axis aligns with the up/down directions. Thus, when a slice
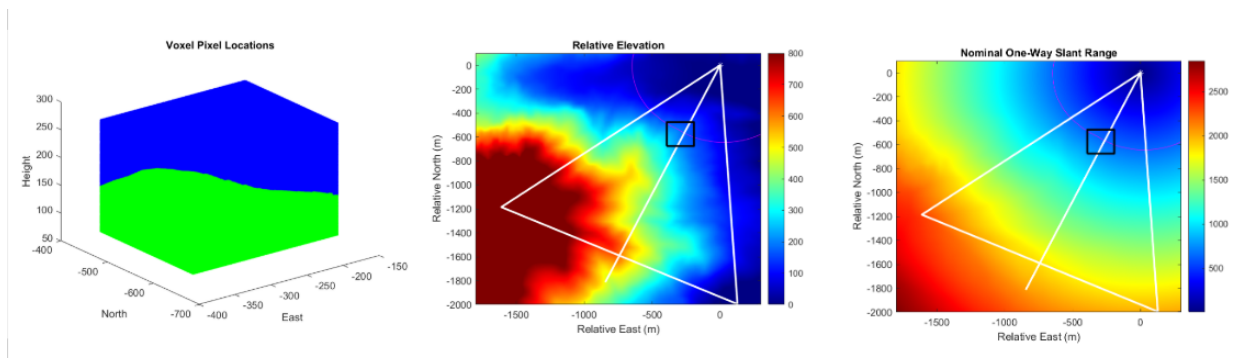
Figure 4.1: Observation site graphics provided for situational awareness. The white lines signify the beamwidth and center line. The black square represents imaging location. The red contour line represents approximate center swath distance. Observation site profile illustrating where to expect voxel locations (*left*). The image is formed 20 meters above to 20 meters below the Digital Elevation Map (DEM) (*middle*). One-way slant range relative to radar location (*right*).
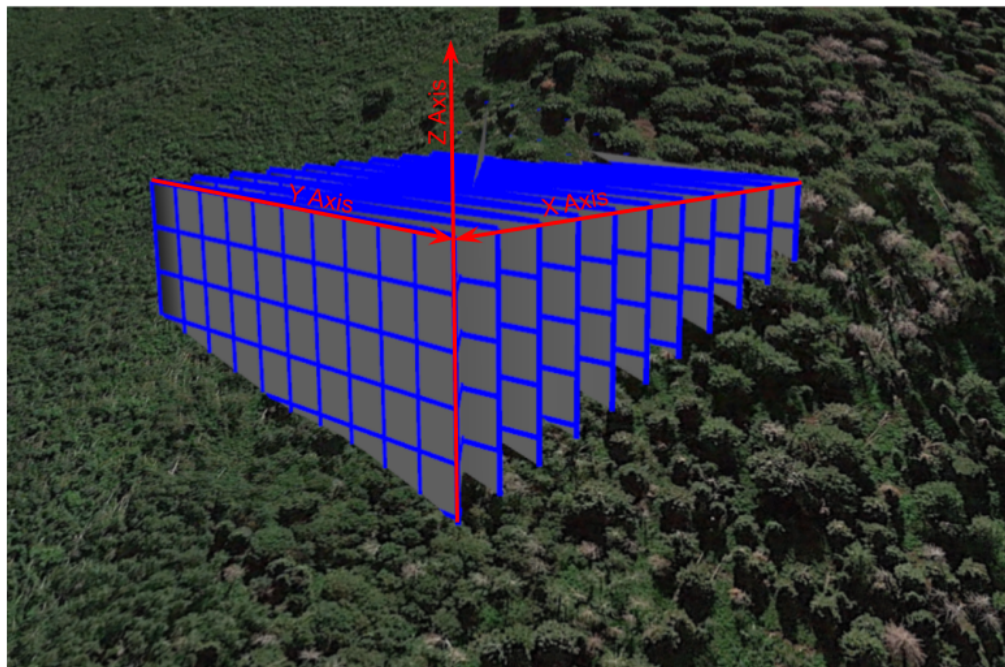
Figure 4.2: An example image cube. The x axis aligns with the east/west directions, the y axis aligns with the north/south directions and the z axis aligns with the up/down directions.

is taken along the x axis, the resulting image provides a profile view of the mountainside. A slice along the y axis provides a head-on view of the mountainside. Finally, a slice in the z axis presents a top down view of the slope. The axis can be seen in Fig. 4.2 alongside an example image cube.

Because these axes align with cardinal directions, they do not align with the radar's axes. As a result, the actual resolution of the image is a projection of the native radar resolution into the image cubes frame. Transforming from the radar coordinate frame to the image cube frame, the resolution becomes .096 m along the y axis (.96 m if slant range resolution is 1 m), 3.42 m in the z axis and 2.4 m along the x axis.

4.2 Results

For this study, imagery is formed at two different resolutions. The images are oversampled to enable cubic voxels, i.e., the voxels have the same length in each dimension. In order to obtain a wide area view of the scene, a coarse resolution tomographic image is formed for the six collections highlighted in Table 4.1. For this imagery, the image cube is 200 voxels in each axis and the voxel's are designated as 1 meter cubes. Thus, these images are 200 m cubes on a side. A second set of tomographic images are then formed using 0.1 meter voxels on a subset of the wide area image. Again, these image cubes are 200 voxels in each dimension, covering 20 m on a side. These two image sets are referred to as the "base imagery" and their characteristics are discussed herein.

Once the base imagery is formed, difference images are formed by comparing the magnitude and phase between two images, consecutive or otherwise. This process is known as change detection. The Change Detection Section focuses on Collection 6 through Collection 9, as these images are all at 0.1 m and have the same minimum slant range. The purpose of this approach is to identify changes between two snowpack states to learn more about snowpack conditions. Change detection reveals snowfall and melt events due to obvious physical differences (more or less snow). Additionally, change detection identifies crystalline structure changes that, when combined with environmental information, reveals further information about the stability of the snowpack.

4.2.1 Base Imagery

The first data set in consideration is Collection 4 which took place on February 26, 2017. The snowpack during this collection is healthy, having received over a meter of snow in the previous two weeks and just shy of six meters for the entire season. The temperatures were, on average, just above freezing during the day and well below freezing during the night. Additionally, the high

41
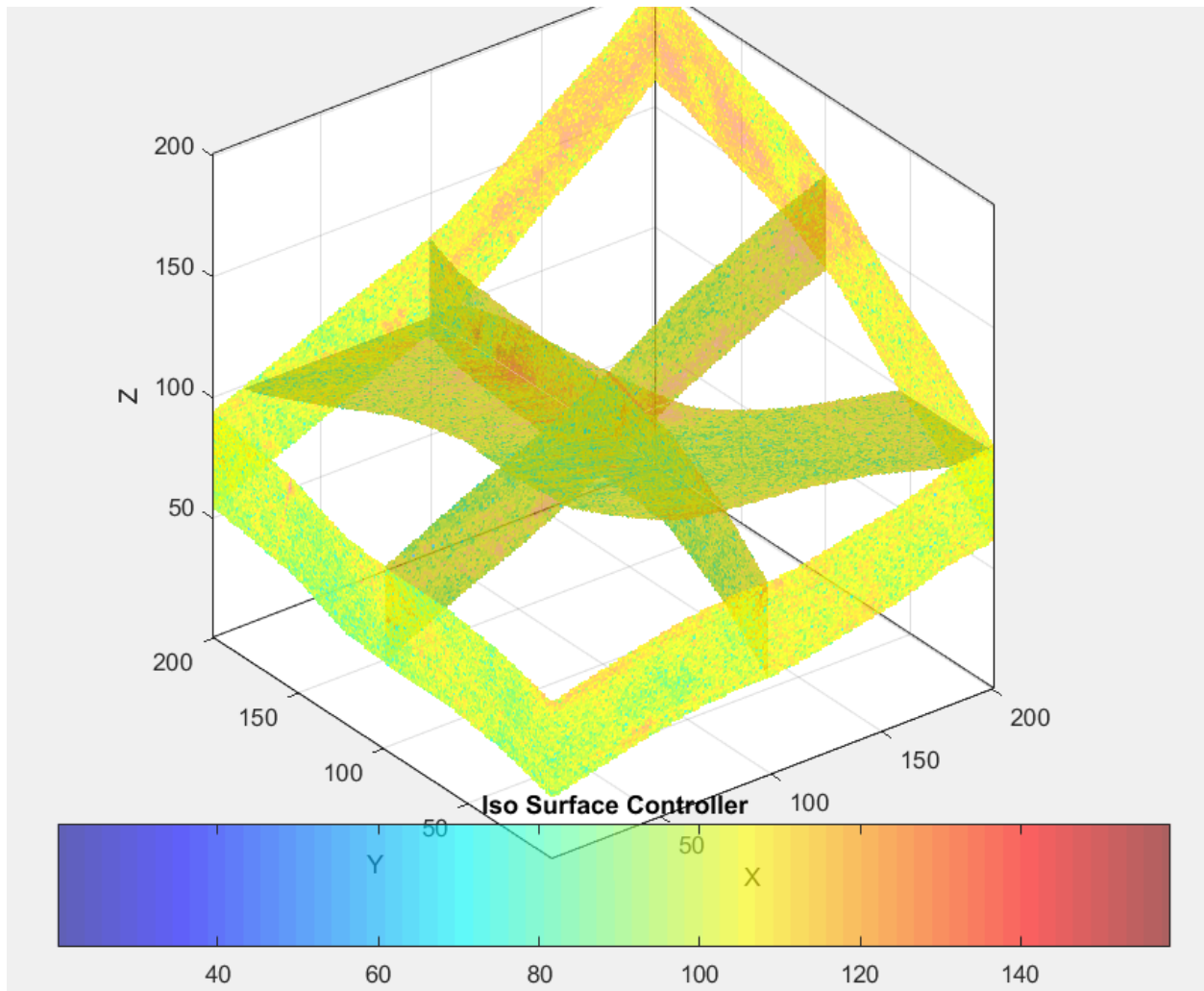
Figure 4.3: Collection 4, 1 m resolution. The tomographic image cube with a slice in each of the three axes down the center. The ground is visible in all images, and follows the elevation map.

on the day of the collect is below freezing. As such, the snow is expected to have a low moisture content.

A coarse resolution image is shown in Fig. 4.3 using seven different image slices along along three axes. Three slices are shown in the x and y directions, while a single slice is shown for the z direction. The ground and snow are clearly visible, most predominantly in the x and y slices at tick 200, which also shows the ground sloping upward matching the topography. The individual center slices are displayed in Fig. 4.4.

A progression of slices, such as in Fig. 4.5, provides a unique perspective of which targets persist within the image. The ground and snow are present across all of the slices. There are also

Figure 4.4: Collection 4, 1 m resolution. The *x*, *y* and *z* slices are displayed from the center of the image individually. A bright red plane is present in each image, which is the ground and snow returns.

Figure 4.5: Collection 4, 1 m resolution. A progression of slices along the *x* axis. The slices are every 50 m within the 200 m cube. Bright returns forming planes are ground and snow returns.

targets with discernible height, most noticeably in the center x slice. However, there are no signs of stratigraphy within the image due to the coarseness of the resolution - this is expected.

Collection 4 is performed using a transmit bandwidth of 500 MHz, which equates to a range resolution of 0.3 m. The imagery shown in Fig. 4.6 are oversampled at 0.1 m. Again, the azimuth and elevation are oversampled to 0.1 m to maintain uniform voxels. Referring back to Fig. 4.3, the image cube in Fig. 4.6 is a 20 m cube extracted from the center point but at a finer resolution.

While the ground and snow are clearly seen in the Fig. 4.6 as the bright returns (red), layering is still difficult to see. Possible layers are indicated by the dotted lines in Fig. 4.7, which presents the center slices, formed at 0.1 m resolution, in the x, y and z directions. Several bright returns are displaying height, which are possible rock or tree targets. The bright red, crisp line, which spans the entirety of each image is an artifact, not a real target.

On March 11, 2017 Collection 5 takes place. Between Collection 4 and 5, almost a half meter of snowfall is recorded averaging 8.0 cm per event. The average low since Collection 4 was well below freezing while the average high settled just above at 0.7 °C. On the day of the collection, the temperature is 6.7 °C which has an adverse effect on the water moisture of the top layers of snow.

Looking to the imagery in Fig. 4.8, Fig. 4.9 and Fig. 4.10 similar traits are displayed when compared to Collection 5 - validation that the system is imaging properly. Again, the ground and snow can clearly be seen in each of the slices. Height is displayed by a target in Fig. 4.8 in the x slice at [200, 150, 170] (top-right side of image). This target is most likely a large tree as it spans tens of voxels in the z direction. While larger targets are clearly visible, fine targets such a stratigraphy or crystalline structure are not visible.

Fine resolution imagery is formed for Collection 5 using 0.1 m voxels and is displayed in Fig. 4.11. The imagery closely resembles that of Collection 4 which is not expected due to the warmer temperatures at the time of the collect. Due to the coarse resolution in the elevation and azimuth direction, targets appeared to be stretched, which creates a layered appearance. However, these apparent layers are orthogonal to the ground which is the wrong orientation. Possible layers are called out in Fig. 4.12. The layers look similar to those shown in Fig. 4.7, which may suggest the returns are permanent structures such as the ground.

Figure 4.6: Collection 4, 0.1 m resolution. Four slices in the *x* direction provide successive profile images along the mountainside, approximately every 7 m. The ground is present in the three right-most images as bright red groups (dotted ovals). The vertical bright line, identified by the arrows along the top, is an artifact.
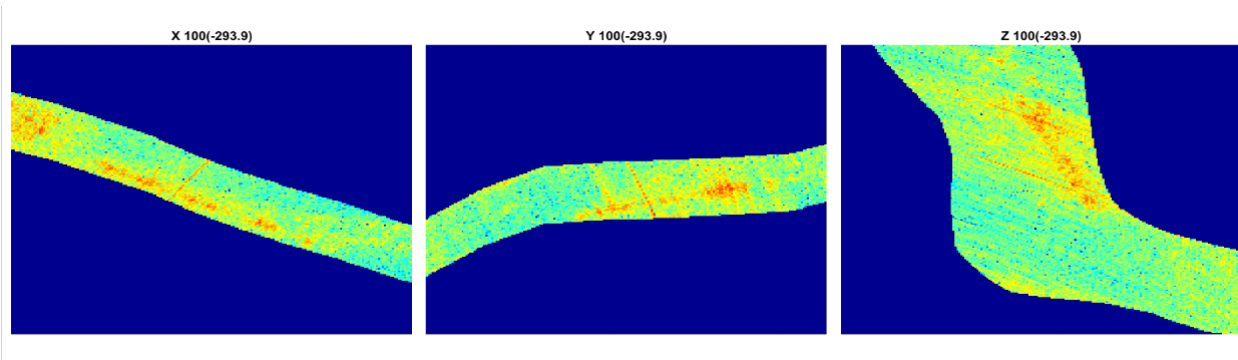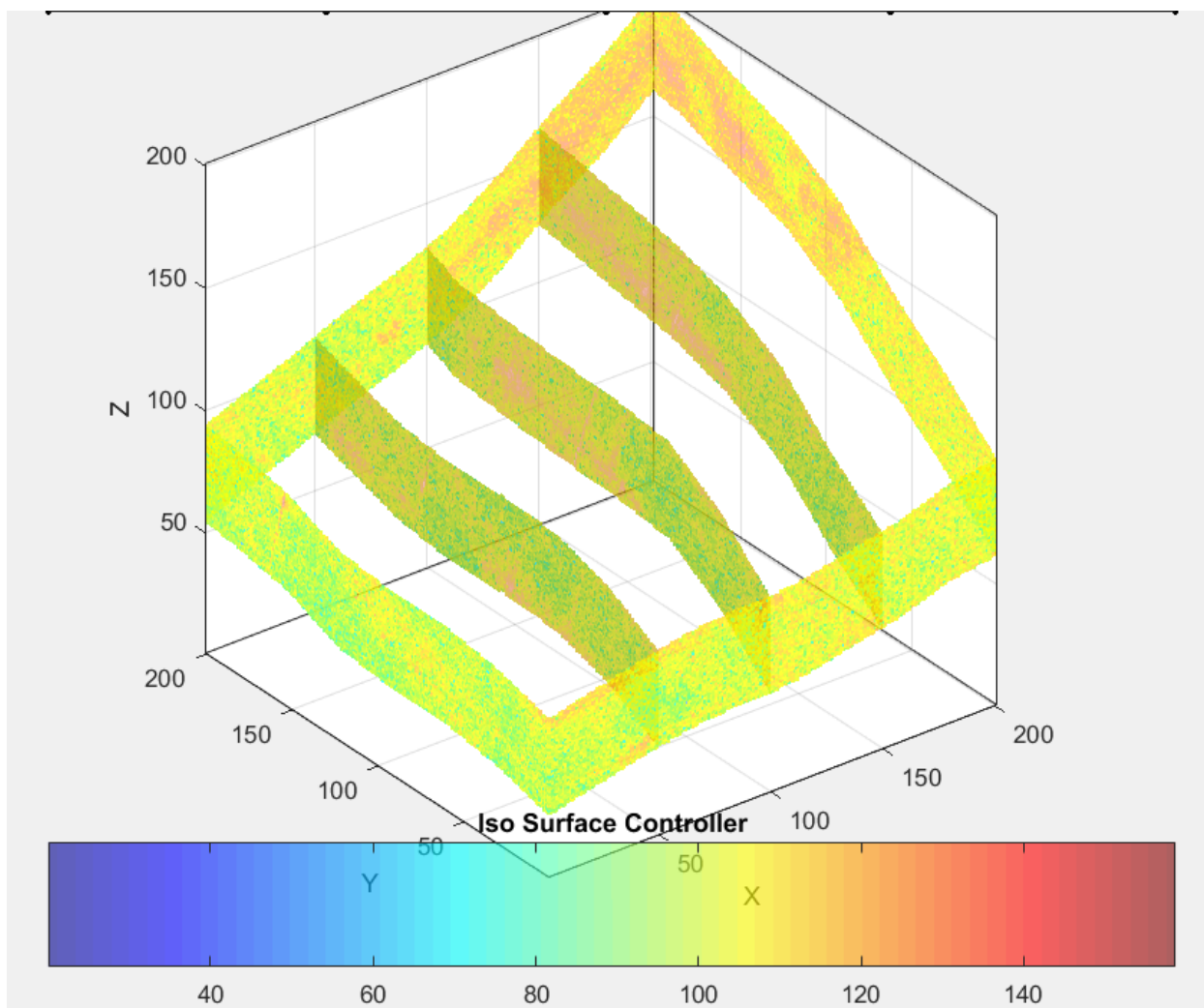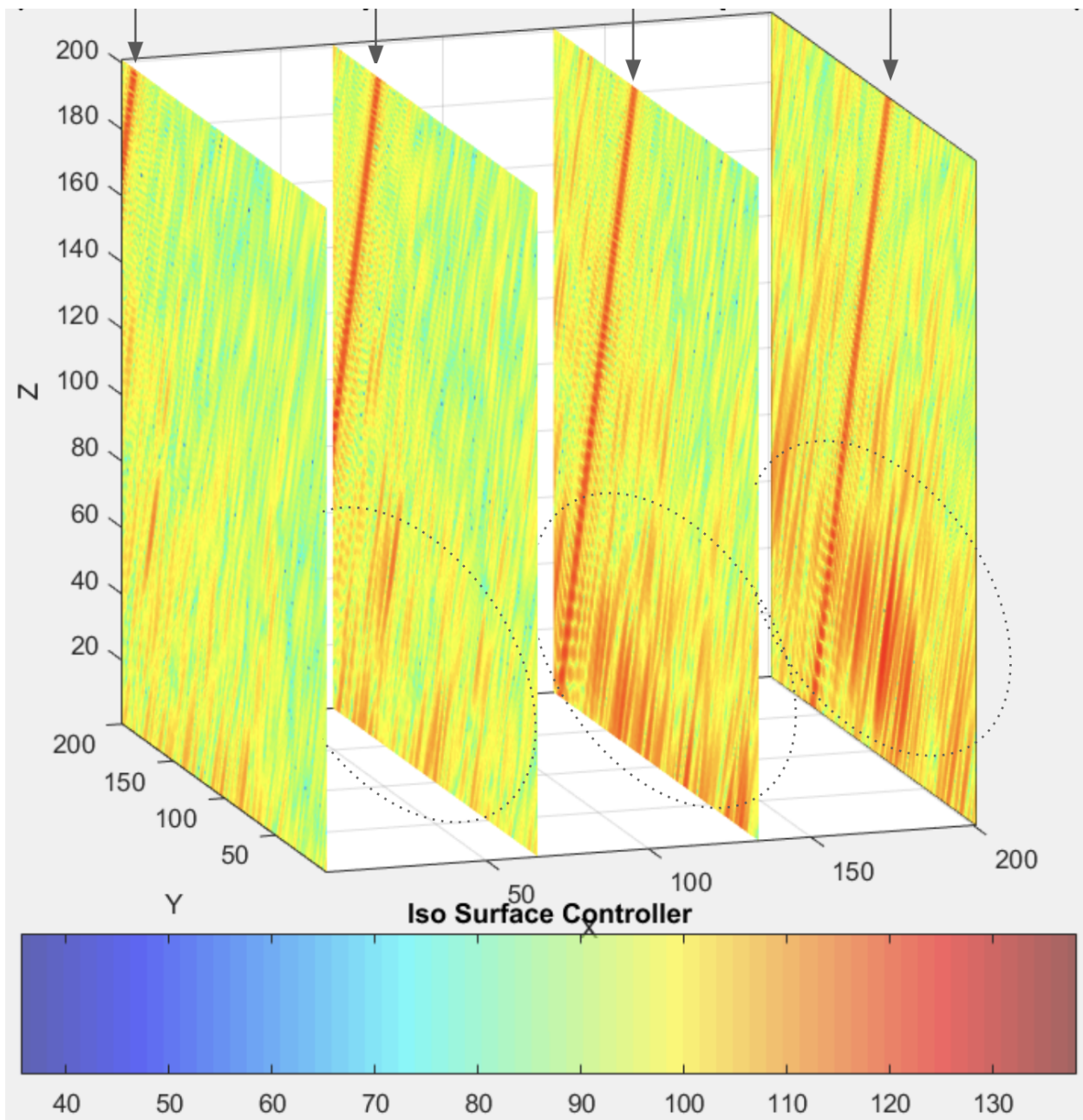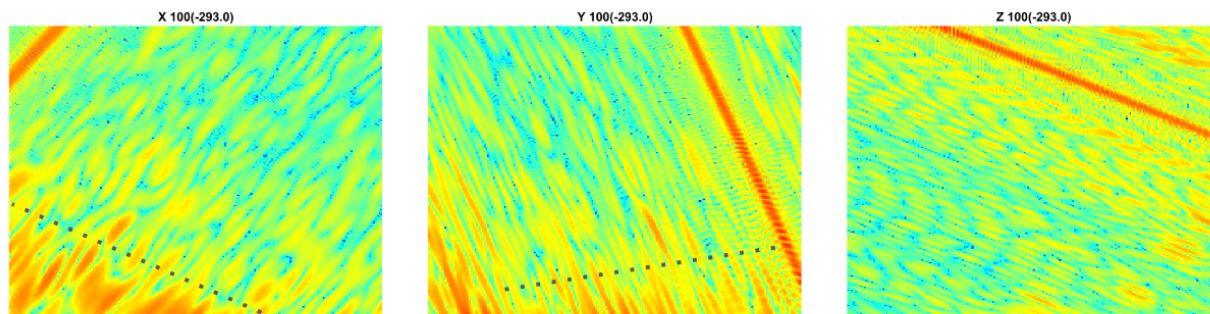
Figure 4.7: Collection 4, 0.1 m resolution. The center slices from each of the three axes are illustrated. Possible layers are indicated by the dotted lines. The layer does not appear in the *z* slice. The bright red line in each image is an artifact.

On March 19, 2017 the first 0.1 m data is taken during Collection 6. There is no recorded snowfall between this collection and the previous collection. Average temperatures well above freezing during the day (11 °C) have contributed to some level of melting and/or settling. Additionally, night-time temperature averages were slightly above freezing. On the day of the collection, the temperature rose to 12.2 °C which results in a higher snow moisture content due to melting.

A coarse image is created and is shown in Fig. 4.13. The Signal-to-Noise Ratio (SNR) is lower for this image than the previous collections. As a result the ground and snow are more difficult to identify. However, it is still present in most of the slices in the figure as a light yellow band.

The ground and snow are most easily noticeable in the *x* slice at tick 200. It is also present in the *x* slice at tick 100, but as *y* increases, the imaging plane drops below the ground. Although each voxel is at the exact same location as the previous coarse images, the characteristics of this image are different. This is likely due to different environmental conditions causing higher snow moisture content resulting more forward scatter (away from the radar) and decreased volume backscatter. Reduced SNR may also be a result of the increased transmit bandwidth.

Fine resolution imagery for Collection 6 is displayed in Fig. 4.14 as series of slices along the *x* axis, providing a sequential profile view. There are no distinct layers present in the imagery. A single possible linear occurrence is visible across each of the images and is in the correct orientation, in agreement with the slope of the mountainside. However, the signature is not strong and may be too faint to convince the reader of its presence.

46
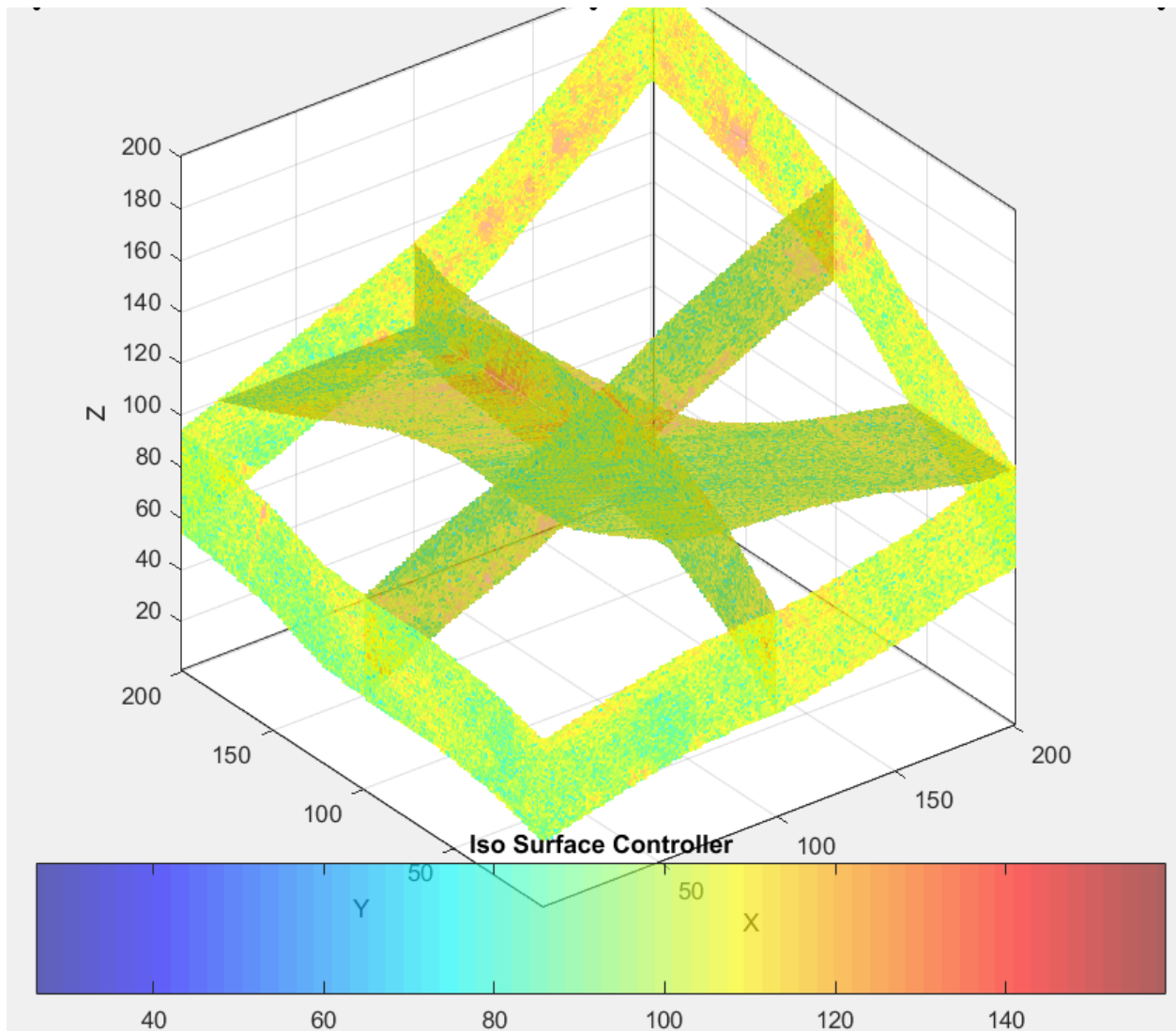
Figure 4.8: Collection 5, 1 m resolution. The tomographic image cube with a slice in each of the three axes down the center. The ground is visible in most of the slices, again following the elevation map.

At the time of Collection 6, the snow pack stratigraphy is extremely complex. Total snowfall exceeds six meters and there have been 48 measurable snowfall events. Average temperatures have fluctuated from -10.2 °C up to 11 °C, so settling and melting have inevitably occurred.

Collection 7 took place on March 24, 2017. Between Collection 7 and Collection 6, 7.6 cm of snow was deposited. Average temperatures were slightly below freezing at night (-1.1 °C) and well above freezing during the day (8.4 °C). On the day of the collect the high temperature of 7.8 °C contributes to an elevated snow moisture content.
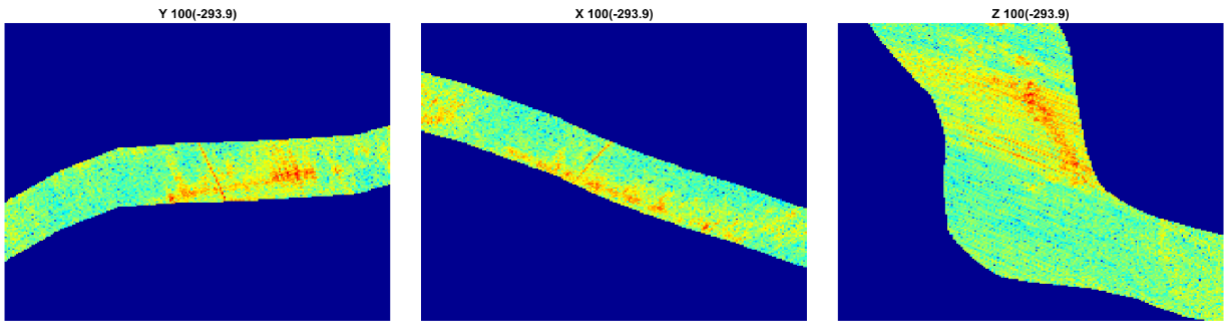
Figure 4.9: Collection 5, 1 m resolution. The *x*, *y* and *z* slices are displayed from the center of the image individually.
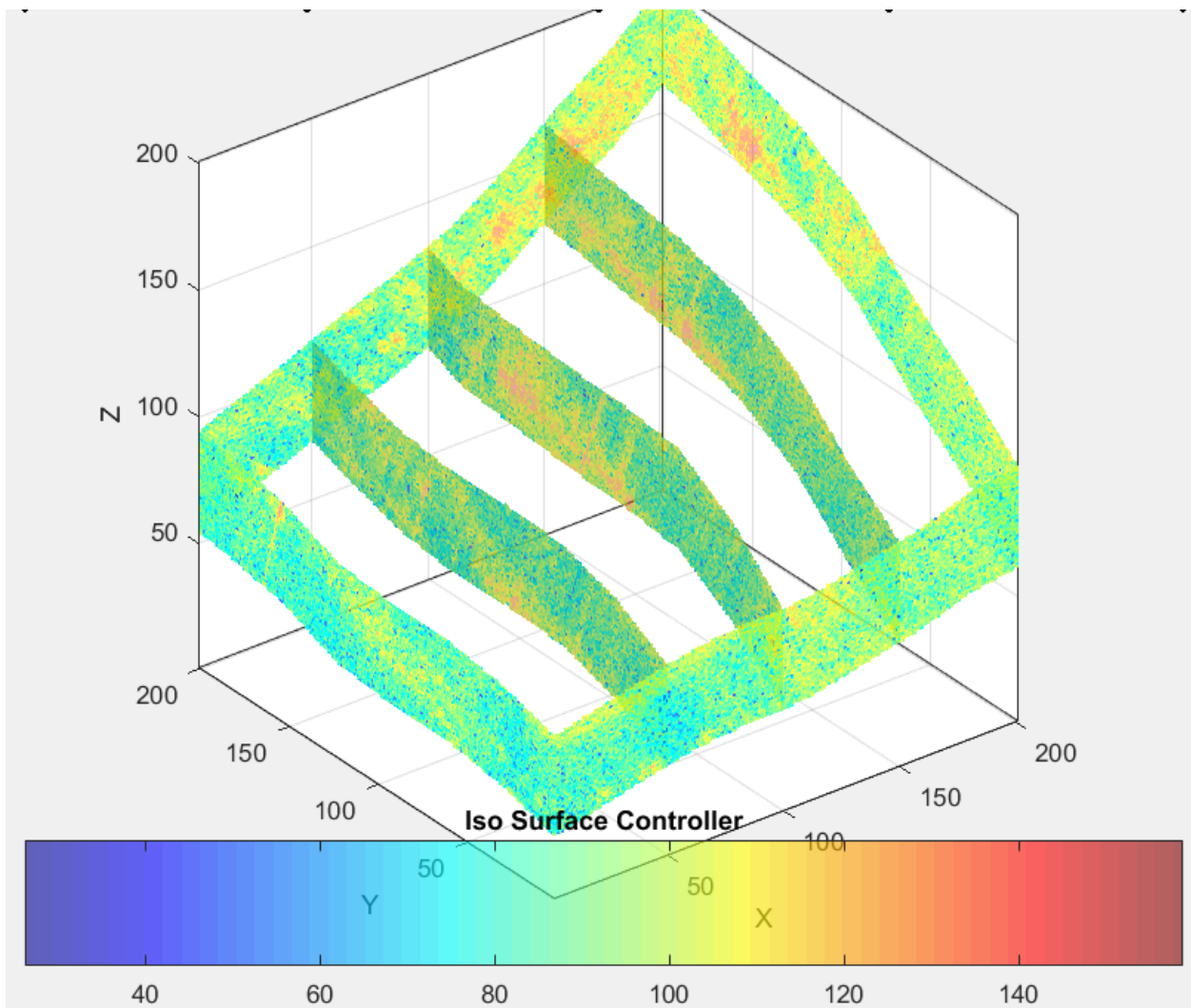
Figure 4.10: Collection 5, 1 m resolution. A progression of slices along the *x* axis. The slices are every 50 m within the 200 m cube. Ground and snow are visible in all slices as a yellow and orange band.
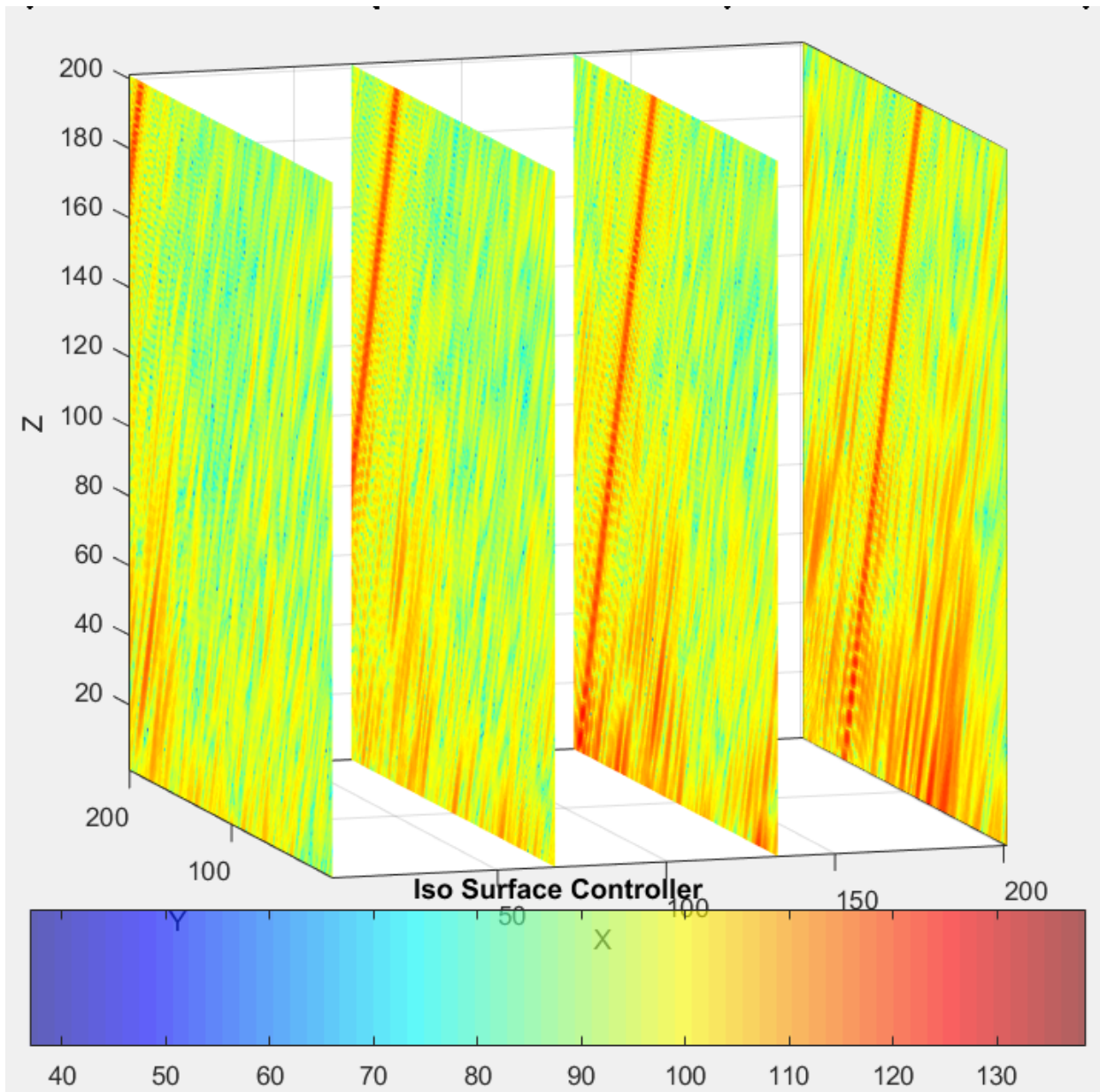
Figure 4.11: Collection 5, 0.1 m resolution. Four slices in the *x* direction provide successive profile images along the mountainside, approximately every 7 m. The ground and snow are present while layers are indiscernible. The bright red line throughout each image is an artifact.
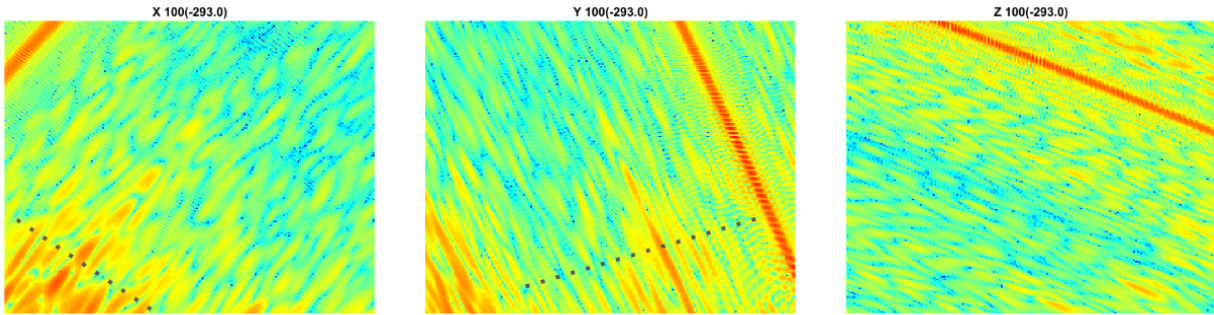
Figure 4.12: Collection 5, 0.1 m resolution. The center slices from each of the three axes are illustrated. Possible layers are indicated by the dotted lines in the x and y slices. The bright red band present in each image is an artifact.

The coarse resolution images are provided in Fig. 4.15 and the fine resolution images are provided in Fig. 4.16. The coarse resolution imagery is similar to the previous images from Collection 4 though Collection 6. The ground and snow are still present in most of the images although at a reduced SNR. This is most likely due to the warm temperature before and at the time of collection causing increased forward scatter and reduced volume backscatter.

The fine resolution image have returns off of several ground targets. These returns are most noticeable in the x slices at 133 and 200 (third and fourth images). The red returns can be seen towards the back of the images at y values of greater than 150 and z values below 100. These targets persist through all the fine resolution images and may be larger objects such as rocks or trees, as opposed to snow.

Another 0.1 m range resolution collection (8) took place on March 25, 2017, just two days after Collection 7. Only 2.5 cm of snow fell during this time frame. Temperatures averaged below freezing at night and well above freezing during the day. On the day of the collect the high is only 2.8 °C above freezing. Thus, the snow is expected to have a higher than desired water moisture content.

In agreement with the previously formed images, major features are visible in both the coarse resolution imagery, Fig. 4.17, and in the fine resolution imagery, Fig 4.18. Minute differences are present in fine resolution image. Along the upper portions of each of the images, for z greater than 140 and y less than 100, there are new bright returns present but there is no sign of distinct layering which should be present.
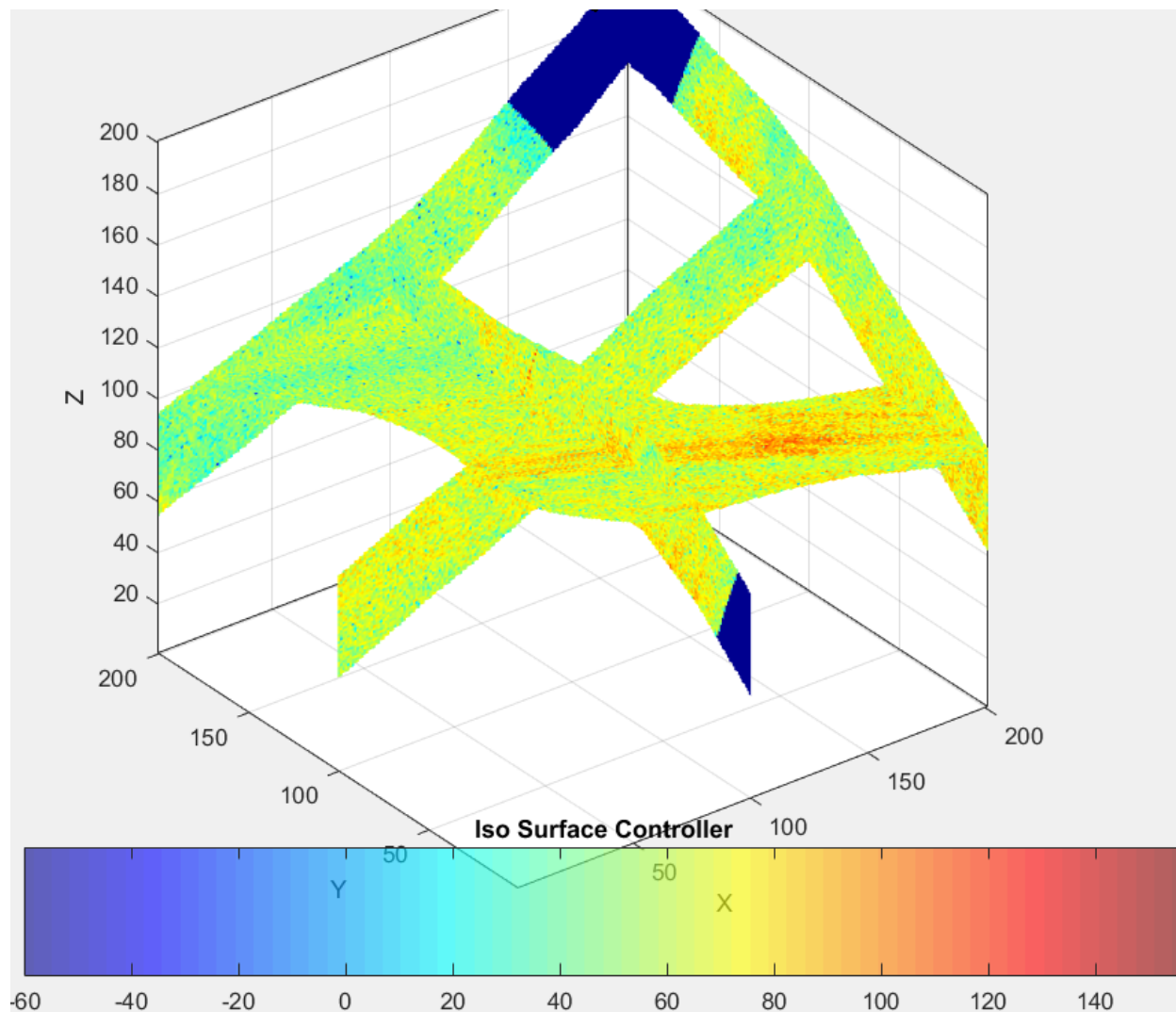
Figure 4.13: Collection 6, 1 m resolution. Slices from each of the three axes are displayed. While the SNR is lower in this image than in previous ones, the ground and snow are present in most of the images as an orange and yellow band.

The final collection in consideration is Collection 9 which took place on April 4, 2017. Between Collection 8 and Collection 9, 20.3 cm of snow fell during two events. The average temperature stayed below freezing at night and was just above freezing during the daytime. On the day of the collection, the temperature does not climb above freezing.

The coarse resolution imagery for Collection 9, shown in Fig. 4.19, looks very similar to prior collections. The ground and snow are present throughout most of the slices. The fine resolution imagery for this collection provides the most interesting features yet when compared to previous collections. Referring to Fig. 4.20, there is far more energy within the scene. While
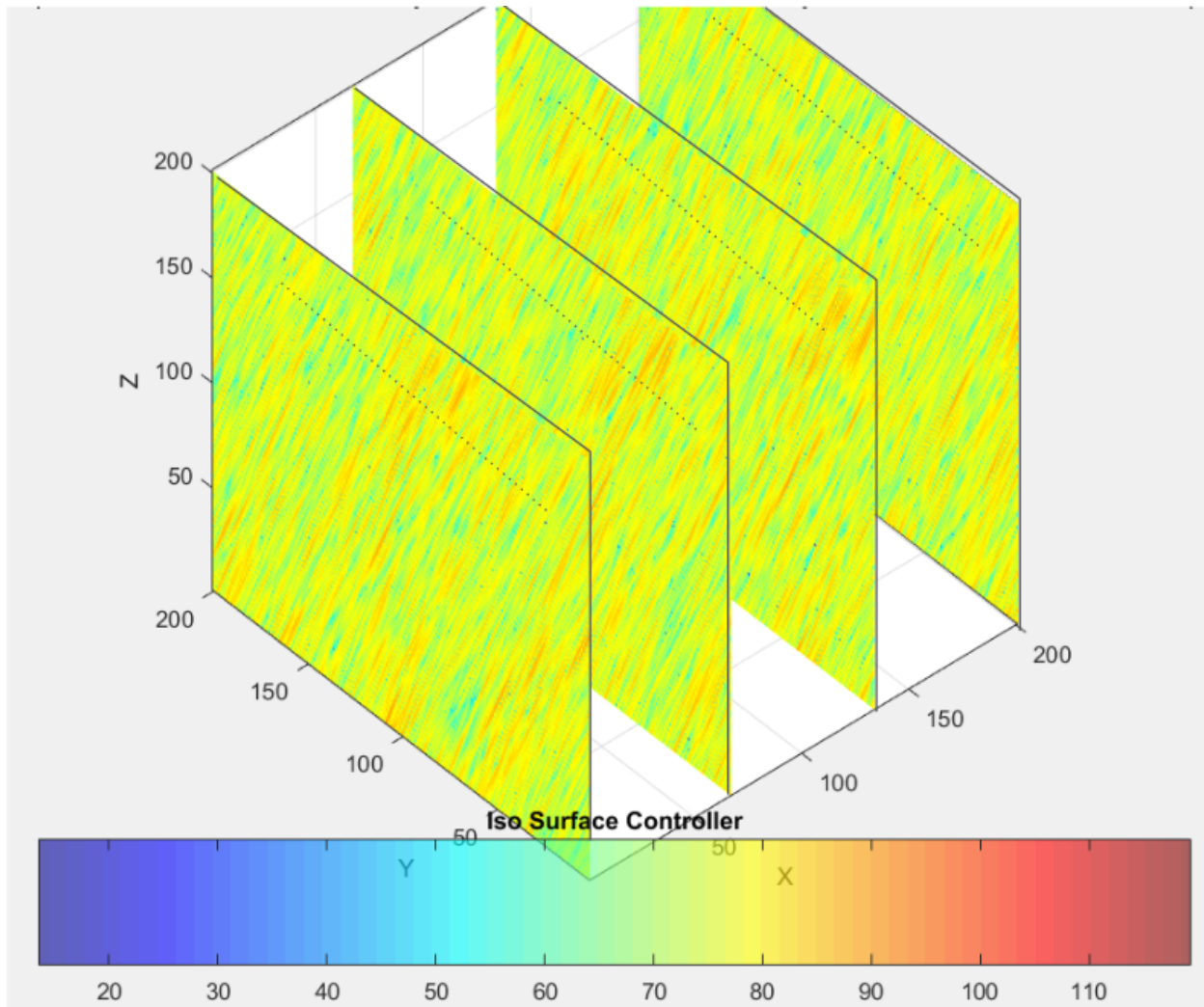
Figure 4.14: Collection 6, 0.1 m resolution. Successive slices in the x direction. Dashed lines identify possible layer across all slices.

identifying distinct layers is a difficult task, a possible layer is identified by the curved line. The progression of this curved line follows the slope along both the x and y axis, in agreement with the the DEM. As this collect occurred late in the snow season, and temperatures have vacillated from well below to well above freezing, the development of this layer most likely correlates to an ice layer within the snow pack.

Figure 4.15: Collection 7, 1 m resolution. Slices from each axis are displayed. The ground and snow are present in most of the images.
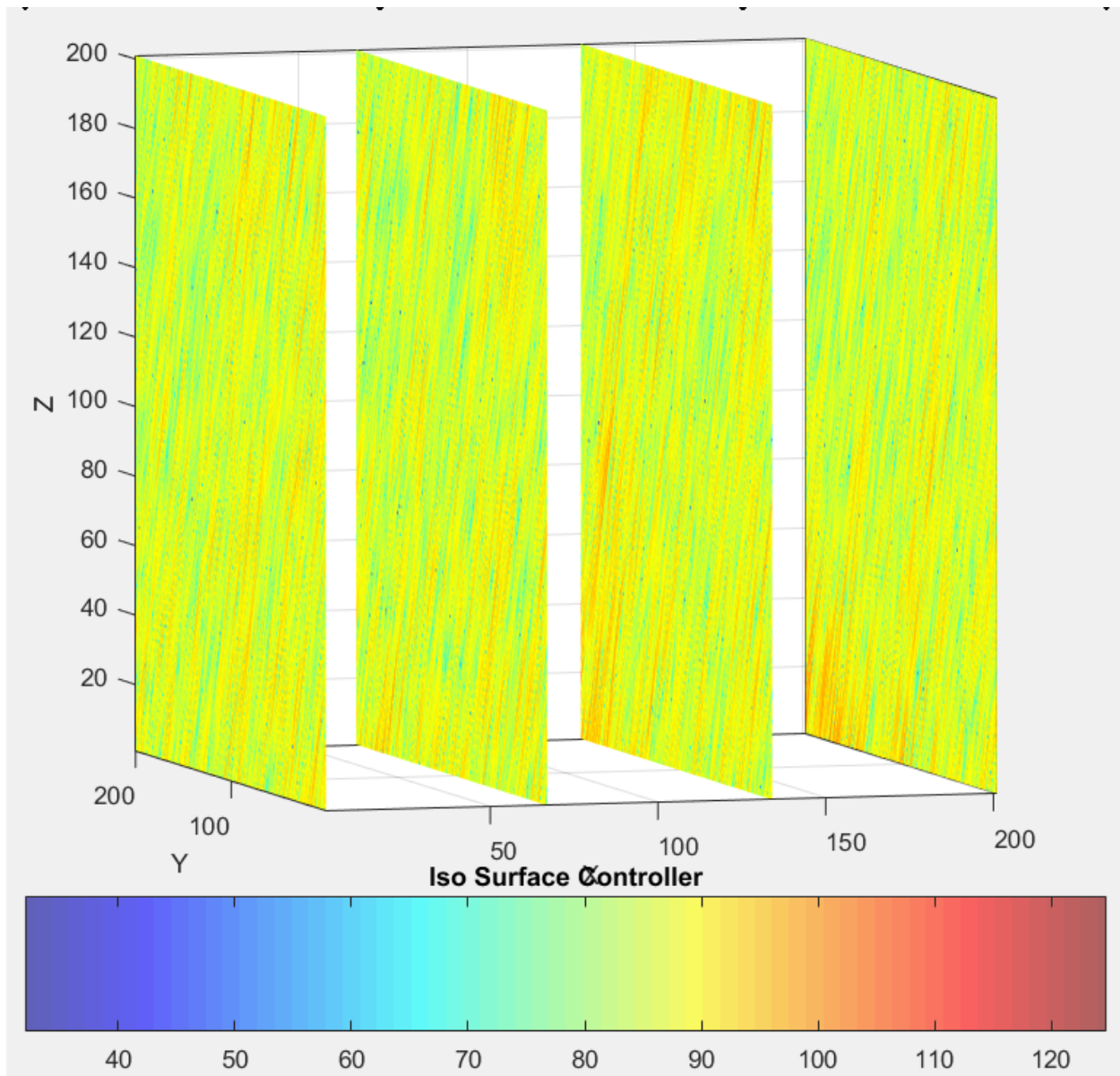
Figure 4.16: Collection 7, 0.1 m resolution. Successive slices in the *x* direction. No clear layering is present in the scene, although targets are present in the bottom right side of the image cube.

Figure 4.17: Collection 8, 1 m resolution. Slices from each axis are displayed. The ground and snow are present in most of the images.

Figure 4.18: Collection 8, 0.1 m resolution. Successive slices in the *x* direction. For *z* greater than 140 and *y* less than 100, there are new signatures present; however no clear layering is apparent.

Figure 4.19: Collection 9, 1 m resolution. Slices from each axis are displayed. The ground and snow are present in most of the images.
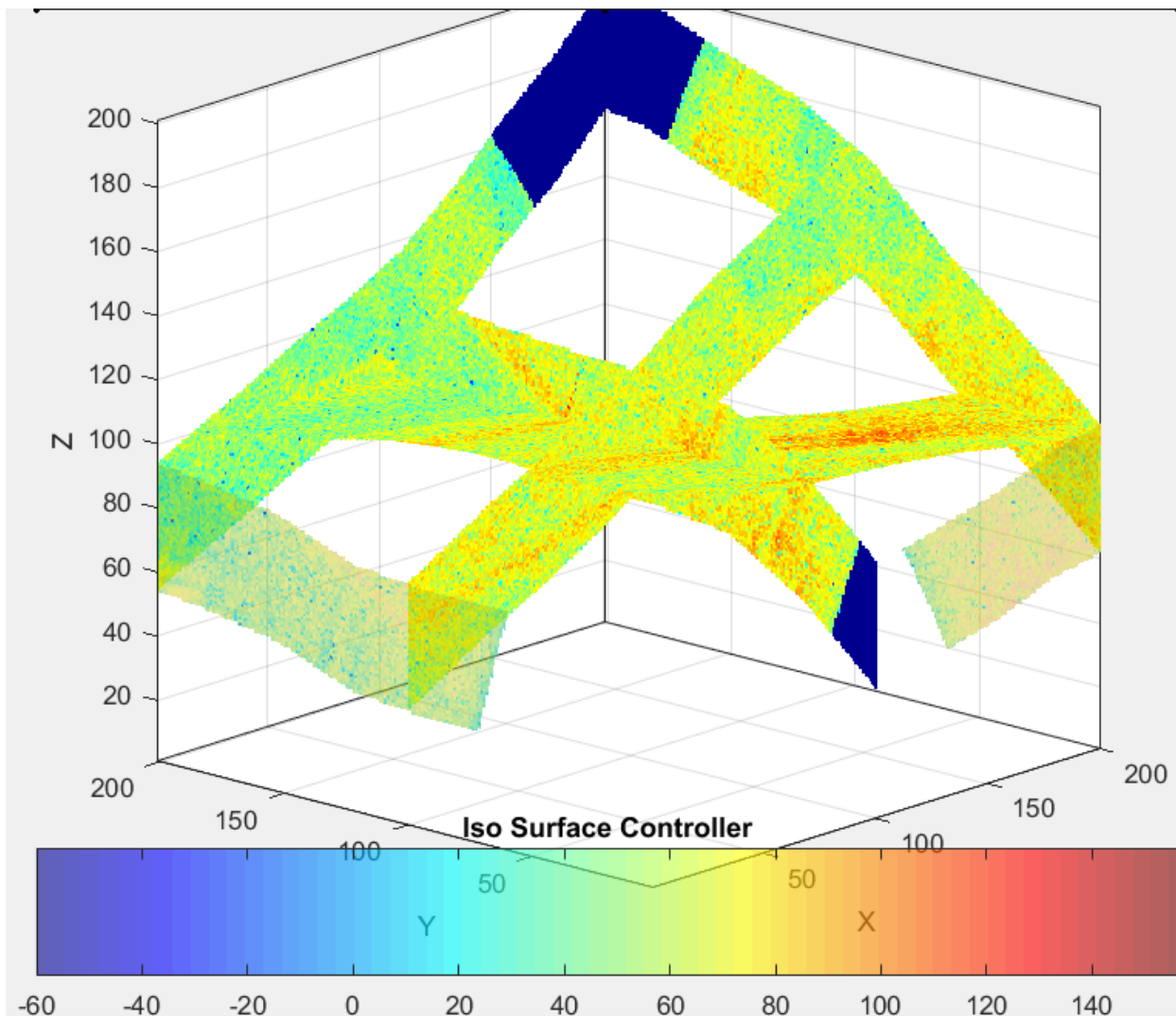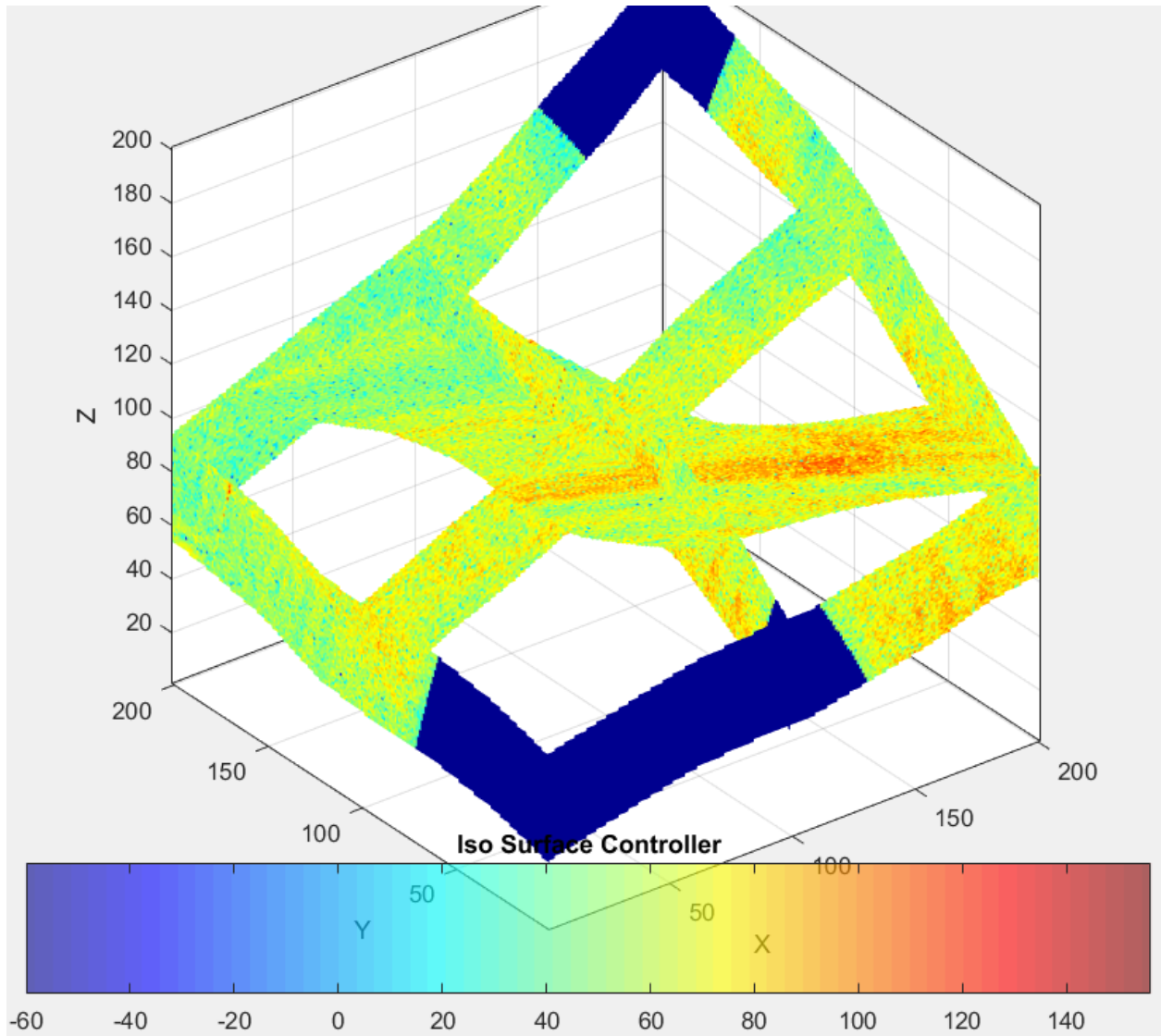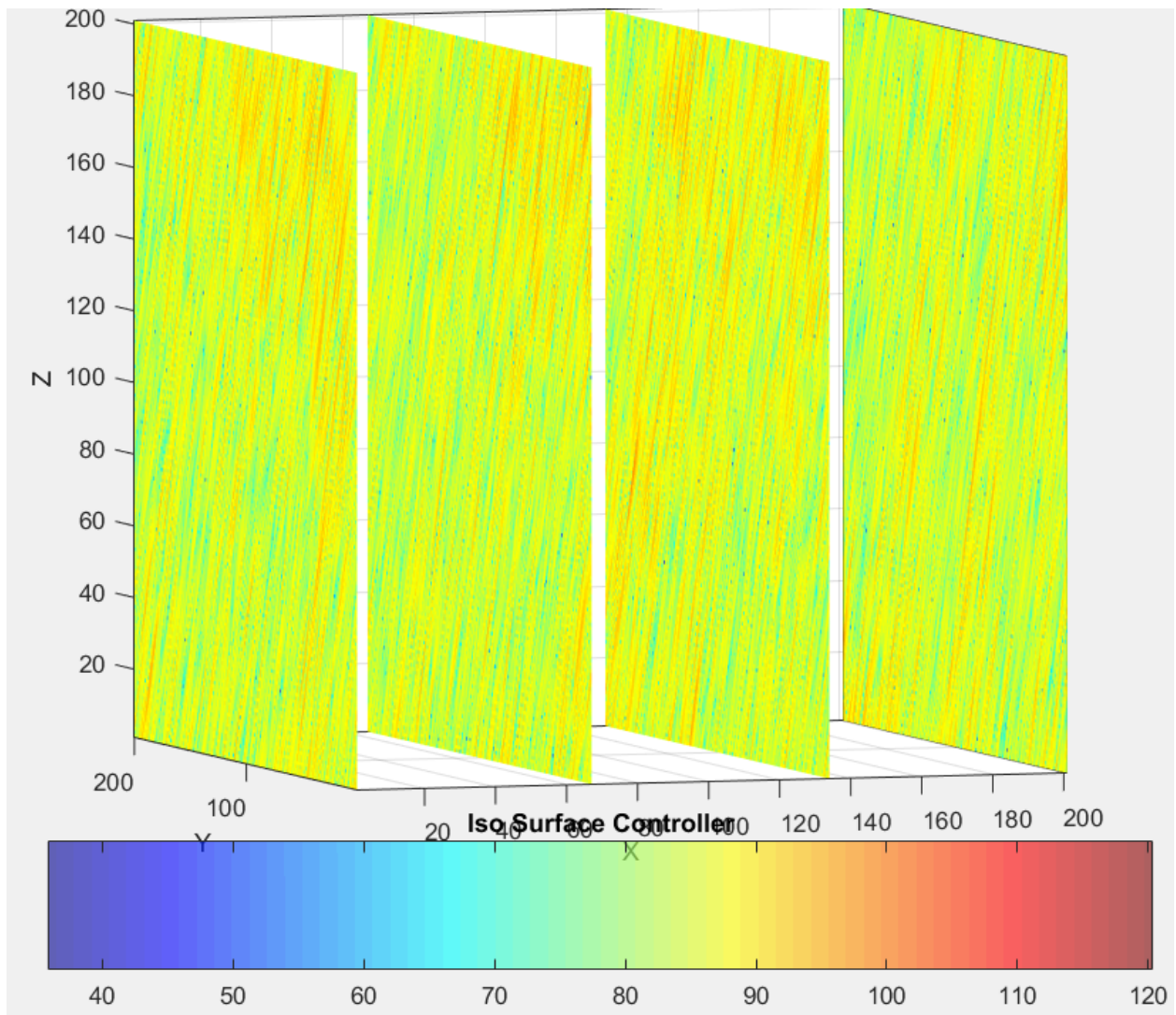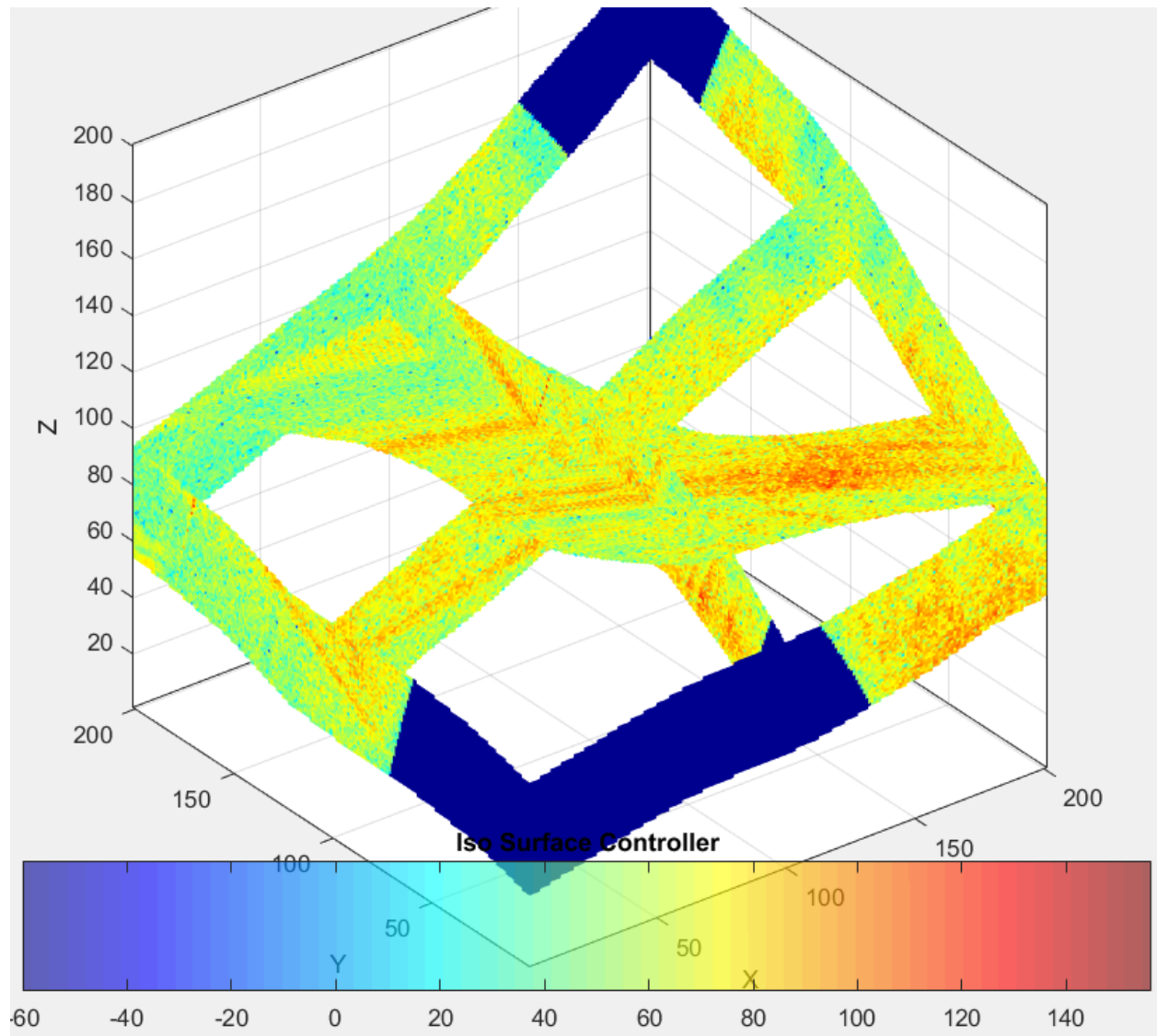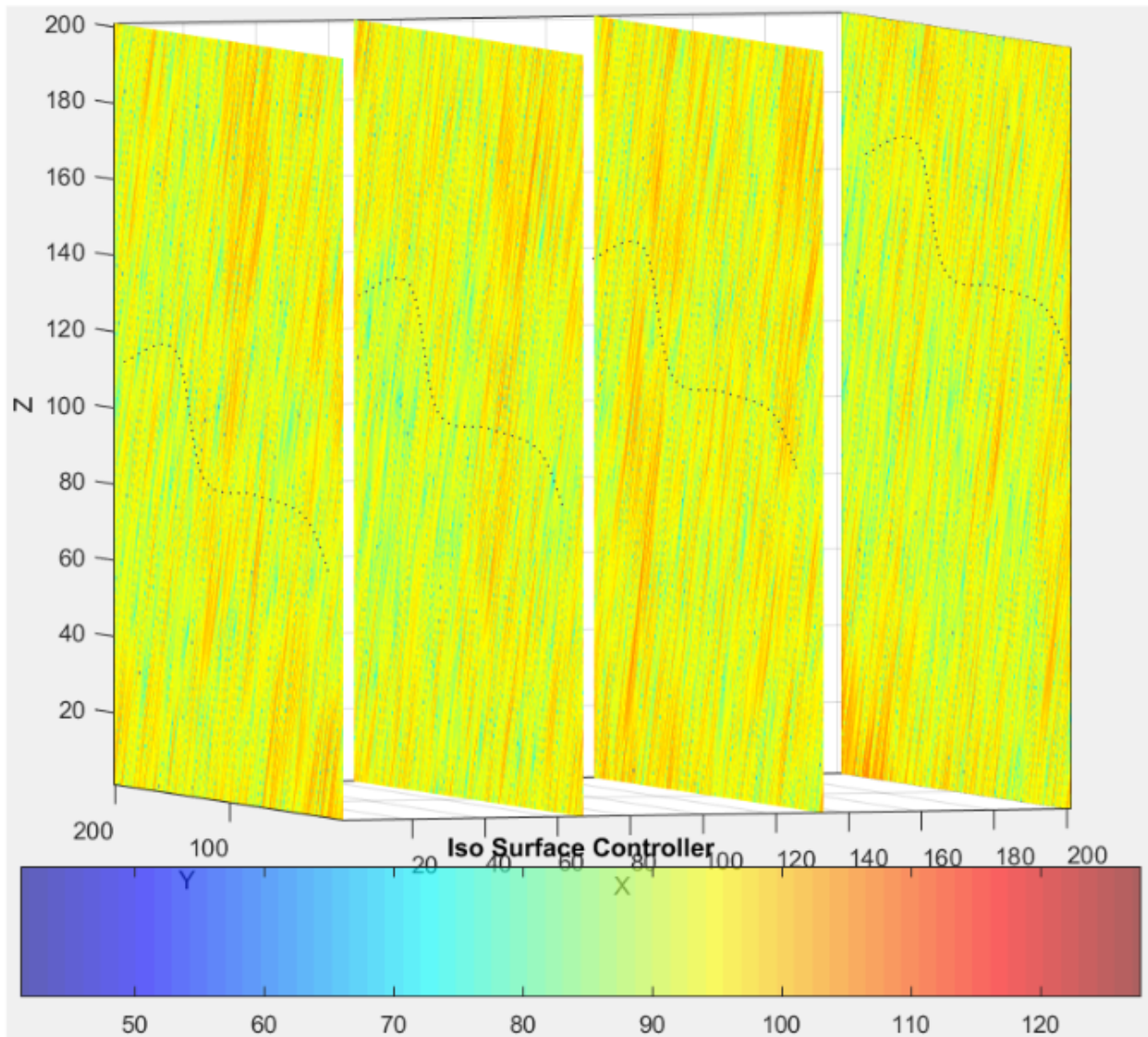
Figure 4.20: Collection 9, 0.1 m resolution. Displayed are successive slices in the *x* direction. The curved, dotted lines signify a possible snow layer, which matches the DEM.

4.2.2 Difference Imagery

The form of change detection performed on the following images is "magnitude change detection". A change detection image is formed by taking a tomographic image and subtracting each voxel from its corresponding voxel in the second tomographic image. Because each of the cubes in Collection 6 through Collection 9 use the same collection parameters and the same image location, each voxel has the exact same relative location from the radar. Additionally, if the scene is completely unchanged, each voxel has the same magnitude and phase response and the difference image is an array of zeros. In practice, the changes in the difference imagery are due to snowfall, snow melt or crystalline structure changes. A summary of snowfall events and average temperatures between base images is shown in Table 4.2 to corroborate changes visible in the following change detection images.

In order to obtain situational awareness, images are created and examined using the coarse resolution base imagery. These images are shown in Fig. 4.21. There are clearly differences between the base collections as revealed by several bands of strong returns in the change detection images (shown in red). As expected, the differences are focused around the ground and snow; however, distinct layers are not present. Inspecting the change detection at the finer resolution should provide more detail about the addition or diminishing of snow layers.

The same method of change detection is used in the formation of the fine resolution difference imagery. The images are provided in Fig. 4.22. There is noticeable change in the x slices above tick 150 (slice 160 is shown in the figure). Unfortunately a distinct layer, or set of layers, is not visible. As there were snowfall events between all change detection images, it is expected that the addition of the material would be obvious. The brightness of the returns does appear to mimic the magnitude of snow deposition. For example, between Collections 6 and 7 there was not much snow fall, and the returns show little change. Conversely, between collections 6 and 9, over 30 cm of snow fell, and the change detection image show noticeably more change occurred (greater amount of red voxels).

In an attempt to decipher if the signatures in the change detection images represent added material (added reflected energy) or diminished material (less reflective energy) the sign of the energy is inspected. The resulting imagery, shown in Fig. 4.23, has a strong ripple in all dimensions. The exact cause of this ripple is unknown, but is most likely due to a small phase difference

Table 4.2: List of change detection images with days elapsed between passes, snowfall events and average temperatures.

Difference Image	Days Elapsed	Snowfall Events	Total Snowfall	Avg. Snowfall	Avg. Temp Low	Avg. Temp High
6-7	5	1	7.6 cm	7.6 cm	-1.1	8.4
7-8	2	1	2.5 cm	2.5 cm	-6.1	3.6
8-9	9	2	20.3 cm	10.2 cm	-5.0	3.4
6-9	16	4	30.4 cm	7.6 cm	-3.9	5.0
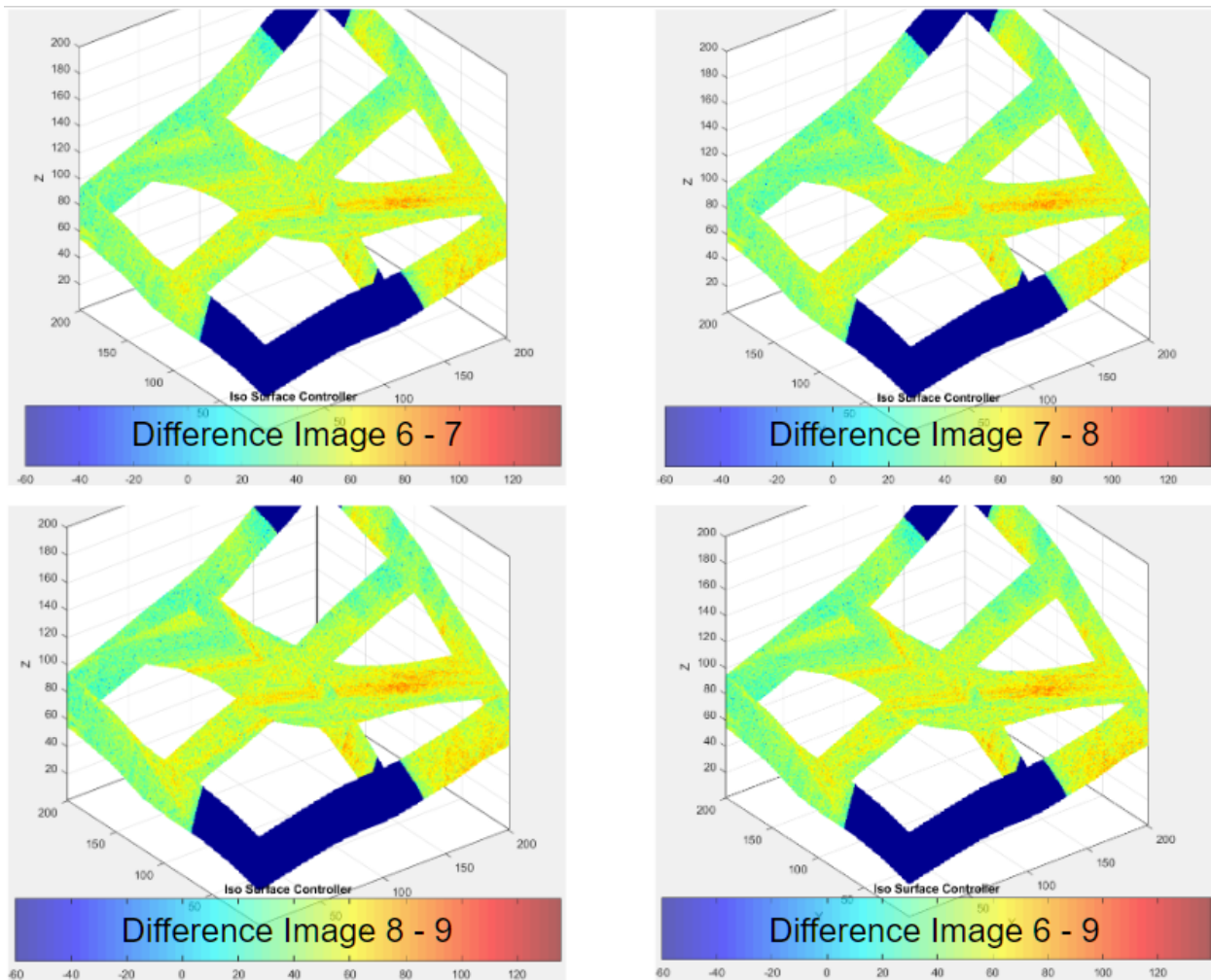
Figure 4.21: Change detection images at 1 m range resolution. Change is evident in each of the images. Red voxels represent a large amount of change, whether that be target energy being added or removed.
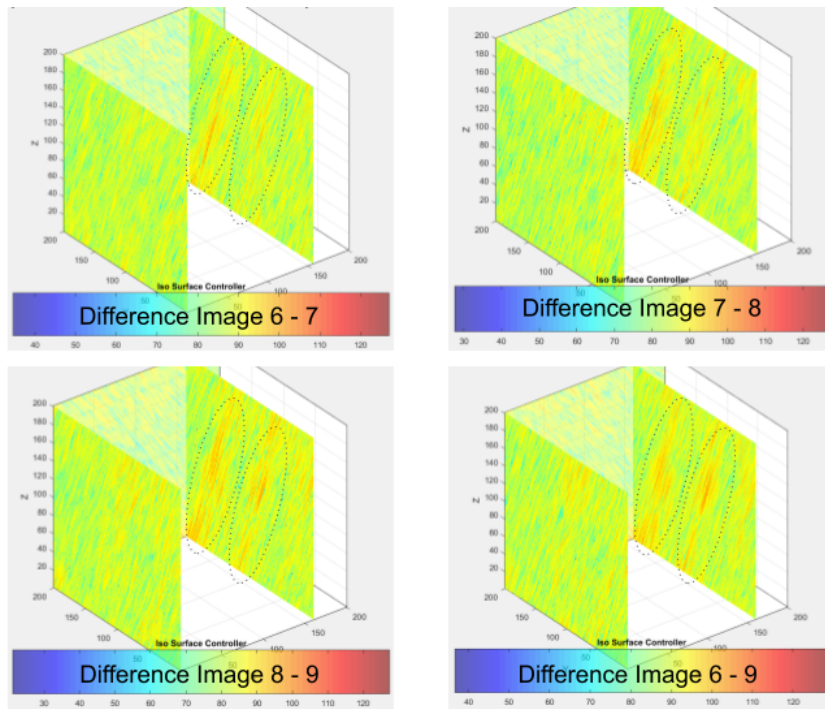
Figure 4.22: Change detection images at 0.1 m range resolution. Slice in the *x* axis are shown at tick 0 and 160. Change is present in the *x* slices greater than 150. Red voxels represent a large amount of change, whether that be target being energy added or removed.

between the two sets of imagery. This ripple is present in all difference images. This phase offset may be caused by antennas being shifted in between passes or by the scanner settling into the soft earth on which it resides, although this is only speculation.

4.3   Conclusion

Data is collected over the course of the 2016-2017 winter at Aspen Grove, Utah. Tomographic images are formed for Collection 4 through Collection 9. Overall, the radar system and scanner appear to be operating correctly as is evidenced by clear targets within the imagery, particularly the coarse resolution base imagery. These images show discernible targets, which in some cases occupy tens of voxels of height. Unfortunately, the fine resolution imagery is not as convincing. Although light layering is visible, there is weak evidence that the resolution is fine enough to reveal stratigraphy.

Magnitude change detection images are formed using the base imagery from Collections 6 through 9. The changes map to where the snow and ground returns are present in the base imagery.
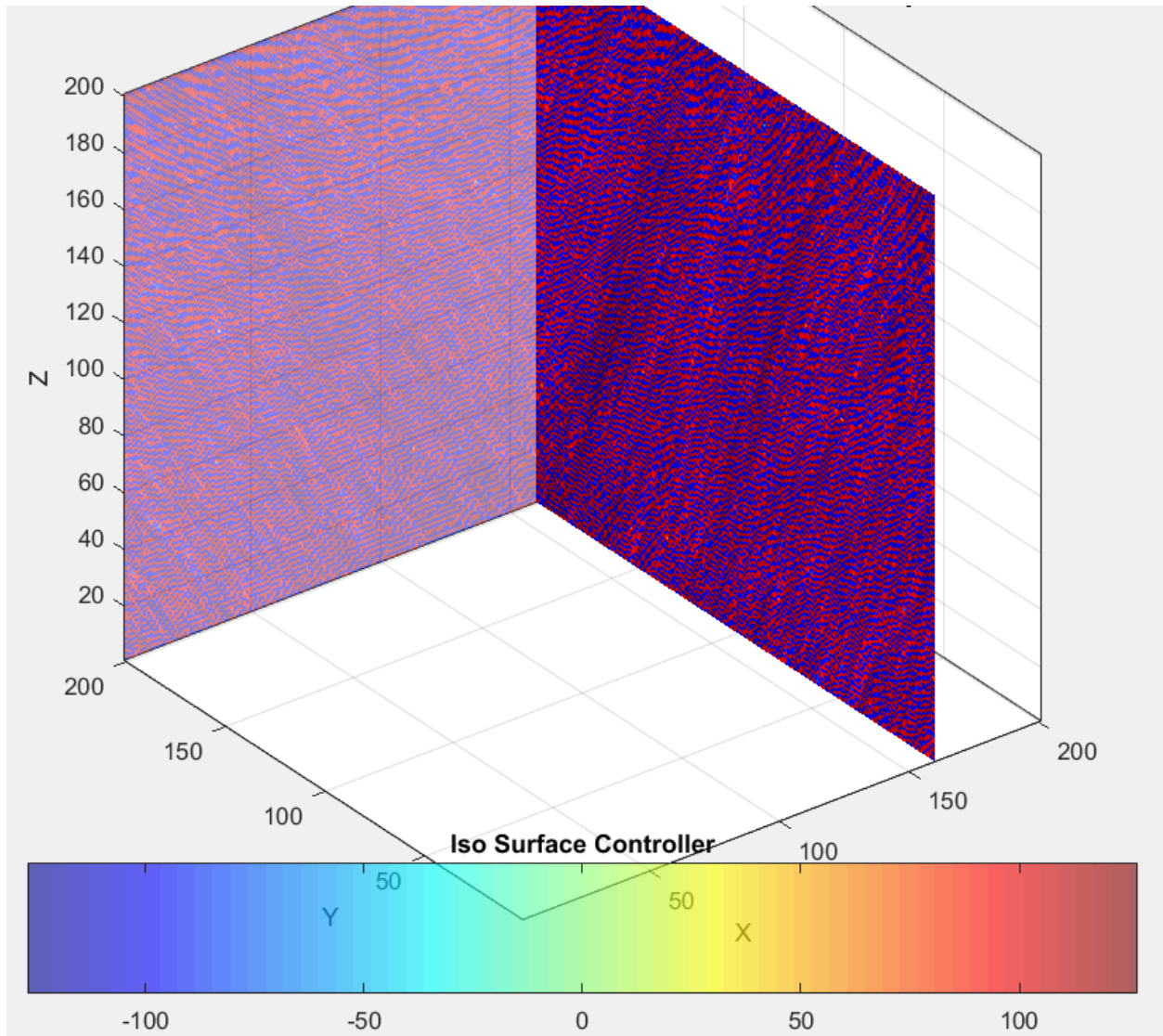
Figure 4.23: Change detection images at 0.1 m range resolution including the sign (positive/negative) of the energy. There is an apparent ripple in the imagery, representing a phase difference between the two images. The cause is unknown.

Again, the fine resolution imagery is not as promising. Although changes are present, they do not clearly reveal stratigraphy within the snow pack. It is speculated that poor image quality at fine image resolution formation is due to the lack of effective resolution, which is caused by the scanning mechanisms limited aperture sizes.

Over the course of the collections, snow deposition averaged 2.5 cm to 10.2 cm for individual snow events. While a 10.2 cm layer may be discernible with a 10 cm range resolution, it certainly is not with the radar systems 3.42 m and 2.4 m resolutions in elevation and azimuth. Due

to the orientation of the scanner, the thickness of the layer is aligned with the radars elevation resolution, presenting a worst-case scenario. Coarse resolution in these dimensions causes perceived smearing, which can obfuscate the relatively thin layering.

Furthermore, the observation site, which was originally thought to be an open meadow, is in fact a heavily shrubbed area. While the area is void of trees, the shrubs cover a majority of the opening and stand .5 to 1 m in height. The shrubs create an unstable layer which the snow resides upon, eventually collapsing sporadically and ruining the homogeneous layers above. As mentioned in the Site Selection Section, a preferred observation area should be bare such that simple, uniform layers are created. This is an unfortunate discovery that is not made until after all data had been collected.

CHAPTER 5.   CONCLUSION

For this thesis a new scanning system was designed and built to provide two dimensional scanning of a radar systems to enable three dimensional imaging of a snowpack. Data was collected periodically during a winter season and processed to create three dimensional images. The results show that tomographic imagery can be formed of a mountainside from a remote location using a high-resolution Ku-band radar and a two dimensional scanner. The scanner and radar operated as intended for the duration of the effort, successfully collecting data with information about the mountainside that would otherwise not have been acquired without placing a human in danger.

High-range resolution imagery was collected throughout the winter season of 2016-2017 at Aspen Grove, Utah. In total, 12 data collections took place at a slant range of 550 to 950 m. These collections cover a comprehensive set of environmental conditions, ranging from no snowfall to heavy snowfall, from temperatures well below freezing to well above.

Using the collected data, tomographic images are formed using the time-domain backprojection algorithm, which when the radar and voxel location are known exactly, form a perfect recreation of the scene. The resultant coarse resolution imagery (1 m range resolution) is of high quality. The ground and snow level are apparent in each collection. Also present in the imagery are large features such as boulders and trees. Again, using backprojection, fine resolution imagery is formed at 0.1 m range resolution. The fine resolution imagery also has large features present but snow stratigraphy is not present.

Finally, change detection imagery is formed to study the addition or melting of snow layers, and reveal changes in snow crystalline structure. Similar to the base imagery results, the coarse resolution change detection imagery is of high quality. Visible changes are present in and around the ground and snow at varying levels. The fine resolution difference imagery also has changes present near the snow and ground returns; however, deposition or melting of snow is not clear in the imagery.

5.1 Contributions

This thesis makes novel contributions to the body of three-dimensional Synthetic Aperture Radar (SAR) imaging. Although the snow condition analysis is limited, this effort provides further insight into the limitations and requirements of a three-dimensional imaging system for interrogating a snowpack.

The Ku-band NanoSAR mounted to a two dimension scanner produced high-quality data at high resolution for several winter seasons (although only one season is discussed). While the slant range resolution is sufficient, the azimuth and elevation limits at long slant ranges are insufficient. Ku-band is a recommended band by several studies [4, 12], because of its ability to both penetrate a snowpack and create high-resolution imagery. However, there are additional facets of a snowpack study that need to be considered.

A new scanning mechanism was designed, built, and deployed. It proved to be effective at creating a two dimension aperture to facilitate three-dimensional images. The design provided accurate location reporting for each radar pulse which is essential for quality SAR imagery. The mechanism operated throughout the course of several winters (though data from only one season is analyzed in this thesis). The scanner worked reliably in extreme environments and made possible the formation of high-quality imagery. Due to its robust design, the scanning mechanism can, and hopefully will be, used for future collections.

5.2 Future Work

While many parts of this effort were successful, there are several steps that can be taken in the future to improve image quality and data utility. First and foremost, the image quality needs to be improved. There are two ways this can be accomplished: increased resolution in azimuth and elevation and improved study location. Furthermore, advanced post-processing techniques should be employed to remove system errors and thus produce the best possible image.

It is believed that the slant range resolution of 0.1 m is sufficient, but that the azimuth and elevation resolutions are insufficient. Referring back to Eq. 2.7, there are several ways which azimuth and elevation resolution can be improved. The frequency of the radar can be increased,

the slant range can be reduced and/or the scanning extents can be increased. Increasing the radar frequency, and thus reducing the wavelength, is not advised as penetration depth is reduced.

Reducing the slant range is the suggested method to increase (make finer) resolution. However, with the current scanning extents, a slant range of approximately 20 m is required to achieve a elevation resolution of 0.1 m, which when seeking to observe a mountainside, is much too short to observe an entire mountainside. Finally, increasing the extents reduces resolution; however, the current scanner is already a large and cumbersome structure. A study in to using different methods to create an aperture and/or materials to make the scanning device lighter will be advantageous.

Selecting a better observation site is key for future studies. The current site presents a complex snowpack due to the heavy foliage. The ability to interrogate a simple snowpack in an alpine environment is important for developing a new radar application such as this. Furthermore, a site which is safely accessible will allow for emplacement of corner reflectors and truth data, which is imperative for validating system health and effectiveness. This effort lacked these key metrics due to the difficulty and danger in accessing the steep mountainside.

Finally, further work should be performed on the existing data. The data collected for this effort is believed to be of high quality and may possess more information about the snowpack which was not extracted in the analysis of this thesis. Suggested algorithmic work includes using auto-focus and multi-look processing to reduced smearing and speckle, which will aid in revealing the snow stratigraphy and crystalline structures.

REFERENCES

[1] Various, 2019. "Sundance Snow History." *Mountain News Report* Available at `https://www.onthesnow.com/utah/sundance/historical-snowfall.html`, Visited 2020-01-02. vi, 35, 38, 39

[2] Various, 2020. "Archival Data." *National Center for Environmental Information* Available at `https://www.ncei.noaa.gov/archive`, Visited 2020-01-02. vi, 38, 39

[3] Holmgren, J., Strum, M., and Yankielun, N. E., 1998. "Extensive Measurements of Snow Depth Using FM-CW Radar." *Cold Regions Science and Technology,* **27**(4-5), pp. 117–130. viii, 12, 13, 14, 15

[4] Preston, S. J., 2010. "Design and Feasibility Testing for a Ground-based, Three-dimesnional Ultra-high-resolution, Synthetic Aperture Radar to Image Snowpacks." Thesis, Brigham Young University-Provo. viii, 1, 2, 7, 8, 12, 13, 14, 15, 17, 18, 21, 24, 65

[5] Hallikainen, M., Ulaby, F. T., and Abdelrazik, M., 1986. "Dielectric Properties of Snow in the 3 to 37 GHz Range." *IEEE Transactions on Antennas and Propagation,* **34**(11), pp. 1329–1340. viii, 16

[6] Ulaby, F. T., and Long, D., 2014. *Microwave Radar and Radiometric Remote Sensing.*, Vol. 0 The University of Michigan Press. viii, 19, 20, 21, 25, 26

[7] Shen, H., and Roper, A., 1970. "Dynamics of Snow Avalanche." *Hydrological Science Journal,* **15**(1), pp. 7–26. 1

[8] Various, 2019. "Colorado Avalanche Information Center." *CAIC* Available at `https://avalanche.state.co.us/accidents/statistics-and-reporting/`, Visited 2019-10-28. 1

[9] Various, 2019. "List of Avalanches by Death Toll." *Wikipedia* Available at `https://en.wikipedia.org/wiki/List_of_avalanches_by_death_toll`, Visited 2019-10-28. 1

[10] Heilig, A., Schneebeli, M., and Eisen, O., 2009. "Upward-looking Ground-penetrationg Radar for Monitoring Snowpack Stratigraphy." *Cold Regions Science and Technology,* **59**(4-5), pp. 152–162. 1, 12, 13, 14, 15

[11] Marshall, H., Schneebeli, M., and Koh, G., 2007. "Snow Stratigraphy Measurements With High-frequency FMCW Radar: Comparison With Snow Micro-penetrometer." *Cold Regions Science and Technology,* **47**(4-5), pp. 108–117. 1, 13, 14, 19

[12] Marshall, H., and Koh, G., 2008. "FMCW Radars for Snow Research." *Cold Regions Science and Technology,* **52**(5-6), pp. 118–131. 1, 2, 12, 13, 14, 18, 65

67

[13] Pielmeier, C., and Schneebeli, M., 1997. "Developments in the Stratigraphy of Snow." *Surveys in Geophysics,* **24**(5-6), pp. 389–416. 1, 12, 14

[14] Yankielun, N., Rosenthal, W., and Davis, R. E., 2004. "Alpine Snow Depth Measurements From Aerial FMCW Radar." *Cold Regions Science and Technology,* **40**(4-5), pp. 123–134. 1, 12, 13, 14, 16

[15] Marshall, H., Koh, G., and Foster, R. R., 2004. "Ground-based Frequency-modulated Continuous Wave Radar Measurements in Wet and Dry Snowpacks, Colorado, USA: An Analysis and Summary of the 200203 NASA CLPX Data." *Hydrological Processes,* **18**(4-5), pp. 3609–3622. 1, 12, 13, 14, 18

[16] Marshall, H., Birkeland, K., Elder, K., and Meiners, T., 2008. "Helicopter-Based Microwave Radar Measurements in Alpine Terrain." In *Whistler 2008 International Snow Science Workshop*, pp. 4220–4223. 1, 13, 14

[17] Richardson, C., Aarholt, E., Hamran, S., Holmlund, P., and Isaksson, E., 1997. "Spatial Distribution of Snow in Western Dronning Maud Land, East Antarctica, Mapped By a Ground-based Snow Radar." *Journal of Geophysical Research,* **102**(B9), pp. 20343–20353. 1, 12, 13, 14, 16

[18] Yan, J., Gomez-Garcia, D. A., McDaniel, J. W., Li, Y., and Gogineni, S., 2017. "Ultrawideband FMCW Radar for Airborne Measurements of Snow Over Sea Ice and Land." *IEEE Transactions on Geoscience and Remote Sensing,* **55**(2), pp. 834–843. 1, 12, 13, 14

[19] Sturm, M., and Benson, C., 2004. "Scales of Spatial Heterogeneity for Perennial and Seasonal Snow Layers." *Annals of Glaciology,* **38**(11), pp. 253–260. 1, 14

[20] Koh, G., Yankielun, N., and Baptista, A., 1997. "Snow Cover Characterization Using Multiband FMCW Radars." *Hydrological Processes,* **10**(12), pp. 1609–1617. 1, 12, 13, 14

[21] Yamamoto, T., Matsuoka, K., and Naruse, R., 2004. "Observation of Internal Structures of Snow Covers with a Ground-penetrating Radar." *Annals of Glaciology,* **38**(11), pp. 21–24. 1, 12, 13, 14, 16

[22] Harper, J. T., and Bradford, J. H., 2003. "Snow Stratigraphy Over a Uniform Depositional Surface: Spatial Variability and Measurement Tools." *Cold Regions Science and Technology,* **37**(3), pp. 289–298. 1, 12, 13, 14

[23] Webb, R. W., 2017. "Using Ground Penetrating Radar to Assess the Variability of Snow Water Equivalent and Melt in a Mixed Canopy Forest, Northern Colorado." *Frontier Earth Science,* **11**(3), pp. 482–495. 1, 13, 14

[24] McDonald, M., 2019. "Heavy artillery, New Technology Key in Preventing Deadly Avalanches in Utahs High Country." *Fox 13* Available at `https://fox13now.com/2017/02/13/world-war-ii-soldier-created-technology-to-prevent-avalanches/`. 2

[25] Damstedt, A., 2019. "Oops! Artillery Overshoot Lands in Neighborhood." *Avalanche Center* Available at `http://www.avalanche-center.org/News/2005/2005-03-23-utah-artillery.php`, Visited 2019-11-15. 2

[26] Richards, M. A., Scheer, J. A., and Holm, W. A., 2010. *Modern Radar: Basic Principles.*, Vol. 0 Scitech Publishing. 8

[27] Duersch, M. I., 2013. "Backprojection for Synthetic Aperture Radar." Dissertation, Brigham Young University-Provo. 10, 12

[28] Doerry, A. W., Bishop, E. E., and Miller, J. A., 2016. "Basics of Backprojection Algorithm for Processing Synthetic Aperture Radar Images." *Sandia Report,* **1**(1), pp. 1–1. 10

[29] Ellerbruch, D., and Boyne, H., 1980. "Snow Stratigraphy and Water Equivalence Measured with an Active Microwave System." *Jounral of Glaciology,* **96**(94), pp. 225–233. 12, 13, 14

[30] Rammer, L., Kem, M., Gruber, U., and Tiefenbacher, F., 2007. "Comparison Of Avalanche-Velocity Measurements by Means of Pulsed Doppler Radar, Continuous Wave Radar and Optical Methods." *Cold Regions Science and Technology,* **50**(4-5), pp. 35–54. 12, 13, 14

[31] Gubler, H., and Hiller, M., 1984. "The Use of Microwave FMCW Radar in Snow and Avalanche Research." *Cold Regions Science and Technology,* **9**(4-5), pp. 109–119. 12, 13, 16

[32] Kanagaratnam, P., Gogineni, S. P., Gundestrup, N., , and Larsen, L., 2001. "High-resolution Radar Mapping of Internal Layers at the North Greenland Ice Core Project." *Journal of Geophysical Research,* **106**(24), pp. 33799–33811. 12, 13, 14

[33] Wiesmann, A., Caduff, R., and Mtzler, C., 2015. "Terrestrial Radar Observations of Dynamic Changes in Alpine Snow." *IEEE Journal of Selected Topics in Applied Earth Observations and Remote Sensing,* **8**(7), pp. 3665–3672. 12, 13, 14

[34] Griessinger, N., Mohr, F., and Jonas, T., 2018. "Measuring Snow Ablation Rates in Alpine Terrain with a Mobile Multioffset Groundpenetrating Radar System." *Hydrological Processes,* **32**(21), pp. 3272–3282. 12, 13

[35] Tebaldini, S., Nagler, T., Rott, H., and Heilig, A., 2016. "Imaging the Internal Structure of an Alpine Glacier via L-Band Airborne SAR Tomography." *IEEE Transactions on Geoscience and Remote Sensing,* **54**(12), pp. 7197–7209. 12, 13, 14, 16

[36] Tebaldini, S., and Ferro-Famil, L., 2013. "High Resolution Three-dimensional Imaging of a Snowpack from Ground-based SAR Data Acquired at X and Ku Band." In *2013 IEEE International Geoscience and Remote Sensing Symposium - IGARSS*, pp. 4220–4223. 12, 13, 14

[37] Reigber, A., and Moreira, A., 2000. "First Demonstration of Airborne SAR Tomography Using Multibaseline L-Band Data." *IEEE Transactions on Geoscience and Remote Sensing,* **38**(5), pp. 2142–2152. 12, 13, 14

[38] Minh Dinh, H. T., Tebaldini, S., Rocca, F., Koleck, T., Borderies, P., Albinet, C., Villard, L., Hamadi, A., and Le Toan, T., 2013. "Ground-Based Array for Tomographic Imaging of the Tropical Forest in P-Band." *IEEE Transactions on Geoscience and Remote Sensing,* **15**(8), pp. 4460–4472. 13

[39] Wu, X., Jezek, K. C., Rodriguez, E., Gogineni, S., Rodriguez-Morales, F., and Freeman, A., 2011. "Ice Sheet Bed Mapping With Airborne SAR Tomography." *IEEE Transactions on Geoscience and Remote Sensing,* **49**(10), pp. 3791–3802. 13, 14

[40] Ash, M., Chetty, K., and Brennan, P., 2010. "FMCW Radar Imaging of Avalanche-like Snow Movements." *IEEE Radar Conference 2010,* **0**(0), pp. 0–0. 13

[41] Ulaby, F. T., and Dobson, C., 1989. *Handbook of Radar Scattering Statistics for Terrain.*, Vol. 0 Artech House. 25